Aalto University
School of Engineering

Joni Sirkiä

Requirements for initial data in photogrammetric recording of rock joint surfaces

Master's thesis submitted in partial fulfillment of requirement for Master of Science degree

Espoo 30.11.2015

Supervisor: Prof. Mikael Rinne
Instructor: M.Sc. Lauri Uotinen

Aalto-yliopisto
Insinööritieteiden korkeakoulu

Aalto-yliopisto, PL 11000, 00076 AALTO

www.aalto.fi

Diplomityön tiivistelmä

Tekijä Joni Sirkiä

Työn nimi Vaatimukset lähtötiedoille kallion rakopintojen fotogrammetrisesta tallennusta varten

Koulutusohjelma Yhdyskunta- ja ympäristötekniikan koulutusohjelma

Pää-/sivuaine European Mining Course (EMC) **Koodi** R3008

Työn valvoja Prof. Mikael Rinne

Työn ohjaaja(t) DI Lauri Uotinen

Päivämäärä 30.11.2015 **Sivumäärä** 83 **Kieli** englanti

Tiivistelmä

Kallion mekaanisen käyttäytymisen mallintamiseen käytettävien parametrien määrittäminen ydinjätteen loppusijoituksen mittakaavassa vaatii suurten in-situ –näytteiden koestamista. Yksittäisestä koestuksesta saatavien tulosten yleistäminen käsittämään alueen kaikkia rakopintoja voidaan kyseenalaistaa. Kallion rakopintojen fotogrammetrinen tallennus pyrkii kehittämään rakopintojen jäljennysmenetelmää suurten rakopintojen ominaisuuksien määrittämiseen pienen mittakaavan rakonäytteistä.

Tutkimuksen tarkoitus oli selvittää kalliorakojen fotogrammetrisen jäljennysprosessin virhelähteitä. Tutkimus suoritettiin analysoimalla pintageometrian muutosta fotogrammetrisen jäljennysprosessin aikana. Tutkimus toteutettiin osana Kallion rakopintojen mekaaniset ominaisuudet (KARMO) -tutkimusprojektia, jonka rahoittajana toimii Valtion ydinjätehuoltorahaston (VYR) kansallinen ydinjätehuollon tutkimusohjelma KYT2018. Työn aineisto kerättiin aiemmin tutkimusprojektille tehtyjen kandidaatintöiden (Pauliina Kallio ja Laura Tolvanen) sekä diplomityön (Eero Korpi) pohjalta. Lisäksi työ koostuu projektin pilottivaiheen raporteista ja muusta tutkimusaineistosta. Aineistoa täydennettiin fotogrammetrisilla lisätutkimuksilla, jotka Pauliina Kallio suoritti.

Diplomityön tutkimukset suoritettiin osittain kirjallisuuskatsauksena, joka keskittyi fotogrammetrisen mallinnuksen laatuun vaikuttavien tekijöiden kartoittamiseen. Lisäksi työssä kehitettiin metriikka pintageometrian muutoksen arvioimiseksi replikointiprosessin aikana. Kehitettyä metriikkaa käytettiin jäljennysprosessin virhelähteiden selvittämiseen. Työn tulosten mukaan fotogrammetrinen replikointiprosessi ei tällä hetkellä kykene luotettavasti jäljentämään alkuperäisen kivinäytteen pintageometriaa. Valumuottien tuotantoprosessissa häviää keskimäärin 2 prosenttia, ja replikanäytteen valuprosessissa keskimäärin 6 prosenttia pinnankarkeudesta. Toisaalta tulokset näyttävät fotogrammetrisen mallinnusmenetelmän toimivan hyvin erityistapauksissa (5/33 näytteessä), ja menetelmä kykenee tuottamaan korkealaatuisia tuloksia pintageometrian mallinnuksesta. Lopuksi työssä esitetään suositus fotogrammetrisen mallinnuksen toteuttamiselle kalliorakojen fotogrammetrisessa jäljennysprosessissa.

Avainsanat Fotogrammetria, jäljentäminen, kalliorako, pintageometria, karkeus, karakterisointi

Aalto University
School of Engineering

Aalto University, P.O. BOX 11000, 00076 AALTO

www.aalto.fi

Abstract of master's thesis

Author Joni Sirkiä

Title of thesis Requirements for initial data in photogrammetric recording of rock joint surfaces

Degree programme Degree Programme in Transportation and Environmental Engineering

Major/minor European Mining Course (EMC) **Code** R3008

Thesis supervisor Prof. Mikael Rinne

Thesis advisor(s) M.Sc. Lauri Uotinen

Date 30.11.2015 **Number of pages** 83 **Language** English

Abstract

Deriving parameters to represent mechanical properties of rock mass in a scale of nuclear waste disposal project requires conducting a large scale in-situ test. Representativeness of one test for a large region of interest is questionable. Photogrammetric recording of rock joint surfaces aims to develop surface replication procedure to offer an alternative for determining mechanical properties of rock joints with laboratory scale testing of rock joint surfaces.

The purpose of this research was to identify errors on photogrammetric replication of rock joint surfaces through evaluation of change in surface geometry during the replication process. The study was conducted as a part of KARMO (Mechanical Properties of Rock Joints) research program, financed by VYR (Nuclear Waste Management Fund) through KYT2018 (Finnish Research Programme on Nuclear Waste Management) research programme. Data for this thesis was compiled mainly from separate bachelor and master thesis works conducted for the research program earlier. The bachelor thesis works were conducted by Pauliina Kallio and Laura Tolvanen, and the master thesis work was conducted by Eero Korpi.

The investigations for this thesis were conducted partly by a literature study that focused on quality of photogrammetric modelling and the factors affecting the accuracy of the model, and partly by developing measuring metrics for evaluation of geometrical change in the replication surface. The developed metrics was applied in a study to clarify the changes undergone by replica models in different stages of the replication process. The results show that the photogrammetric replication of rock joint surfaces is unable to reliably replicate the original rock surface. An average result for a replica sample is to lose 2 percent of surface roughness on casting mold production, and to lose 6 percent of surface roughness in casting of replica sample. The results also show that the photogrammetric modelling procedure works well in special cases (5 out of 33 samples), and is able to produce high quality results for modelling a surface digitally. Finally the thesis presents a recommendation for photogrammetric configuration to be used in photogrammetric replication of rock joint surfaces in the future.

Keywords Photogrammetry, recording, rock joint, discontinuity, roughness, characterization

Foreword

I want to thank the project management team for their efforts in guiding me towards the desired destination. Thank you Lauri, and thank you Mikael!

I'd like to thank the research and support staff contributing to the project as well, without you I would have had nothing to work with. Thank you Pauliina, and thank you Otto!

I'd also like to express my thanks to the coworkers at the article factory for maintaining a relaxed, motivated and most of all enjoyable working environment. Thank you Mattheus, thank you Frans, and above all, thank you Jari-Matti!

Finally, I'd like to thank my crew for support and encouragement over the course of the project, especially you, Iiris!

Espoo 30.11.2015

Joni Sirkiä

Table of contents

Abbreviations

BA	Bundle Adjustment
CMVS	Clustering Views for Multi-view Stereo
DEM	Digital Elevation Model
DLT	Direct Linear Transformation
DOF	Depth of Field
DOG	Difference of Gaussian
DTM	Digital Terrain Model
ISFM	Incremental Structure from Motion
JRC	Joint Roughness Coefficient
KARMO	‘Mechanical Properties of Rock Joints’ research project
LSE	Least Squares Estimation
PCA	Principal Component Analysis
PLY	Polygon File Format
PMVS	Patch-based Multi-view Stereo
SFM	Structure from Motion
SIFT	Scale Invariant Feature Transformation
STL	Stereolithography File Format
SVD	Singular Value Decomposition
TIN	Triangular Irregular Network

1 Introduction

Measuring in-situ shear strength of a rock joint requires conducting a large scale test with massive capital investment requirements, but this is not necessarily how it needs to be. Photogrammetric replication of rock joint surfaces offers one alternative method for determining mechanical properties for a rock joint and evaluating shear strength of the rock joint in a cost efficient way without excessive effort. In this approach, rock joint geometry is captured with photogrammetry, modelled with computer vision algorithms, 3D mold for surface replica is printed and replica samples are casted with concrete. The replica samples can then be tested for shear strength in a laboratory. However, the scaling of a rock joint affects shear strength in a way which is not currently fully understood. The general belief is for scale effect to be negative (Bandis et al. 1981), so that shear strength decreases with increasing sample size. However, some studies have presented results that are inconsistent with this view (Hencher et al. 1993; Kutter & Otto, 1990). With this disagreement of studies, scale effect is still an issue of debate (Tatone & Grasselli, 2012)

While photogrammetric replication is a potential approach for determining mechanical properties for rock joints, photogrammetric process has error sources, which without compensation, result in changes in joint surface geometry. By defining the errors and uncertainties related to the replication process, the change in the geometry can be assessed and to be accounted for in the replication process. Potential error sources in the process are for example accuracy of applied photogrammetric modelling, accuracy of 3D printing, changes in the composition of used concrete and changes in the curing process of the concrete. If loss of geometry can be effectively managed in the process, one could accurately scale and replicate rock joints.

Photogrammetric replication requires a technique to digitalize surface roughness and to produce replica samples for laboratory shear testing from a larger joint sample. Uotinen et al. (2015) presents such a method, and introduces pilot testing procedure for inspection of scale-effect on photogrammetric replication of rock joint surfaces. This method involves photogrammetric digitalization of a joint sample, subsampling the captured joint surface into scaled sample geometries, printing a casting mold for scaled

geometry, casting a replica sample from scaled geometry and shearing the replica sample with a laboratory shear testing procedure.

Barton & Choubey (1977) have performed similar tests before on scale effect for shear strength using self-weight sliding tests on blocks with thoroughgoing joints. In this test setup large samples have been tested first, then sawn into smaller parts and shear tests performed again (Barton & Choubey, 1977). Photogrammetric replication is able to test arbitrary surface scale or synthetic surface geometry and eliminate abrasion effect of earlier tests on sub-samples. This could decrease scatter in the results and thus improve accuracy of results from testing.

This thesis is part of KARMO (Mechanical Properties of Rock Joints) research project conducted by Aalto University's research group for Geoengineering. The KARMO project aims to produce parameters required for modelling mechanical properties of rock joints which can be applied to evaluation of different acceptability criteria and applicability of modelling of displacement analysis for rock joints in design of rock caverns. The primary goal of KARMO project is to develop an independent method for defining mechanical properties of rock joints for numerical modelling with laboratory scale replication series.

In KARMO I, first part of KARMO project, a method for photogrammetric replication of rock joints surfaces was produced, and small scale tests on mechanical properties of joint surfaces for replicated samples were conducted. KARMO II continues to develop photogrammetric method produced in KARMO I. In the first stage of this development process produced sample molds and replication samples were photographed and modelled to digital 3D models. Data produced with this photogrammetric process is analyzed in this thesis to find out how quantity and quality of initial data reflects on confident of results from replication process. Furthermore, the process is to be developed to minimize error and loss of information in the process.

Goals for this thesis are split to three parts. The first part is to identify errors related to developed photogrammetric replication process. The second part is to develop a method for measuring digital accuracy of photogrammetric replication of rock joint surfaces. The third, and final, part is to formulate a recommendation for imaging configuration and photogrammetric processing on photogrammetric replication of rock joint surfaces

by accessing effects of quantity and quality characteristics on produced errors on the replication process. Through this process, this thesis is to define requirements for initial data for photogrammetric replication of rock joint surfaces.

This work concentrates on evaluation and development of photogrammetric replication process developed on KARMO research project. First part of the thesis focuses on the theoretical background of photogrammetry and quality of digital model by conducting a literature research for errors in the photogrammetric modelling process. The second part of the thesis focuses on development of measuring metrics for analysis of the quality of the replication process. The third and last part of the thesis concludes findings from pervious parts into a recommendation for imaging configuration. The evaluation of the principles presented here are limited to the photogrammetric replication of rock joint surfaces in KARMO research project.

The thesis is split into following sections: Chapter 1 presents an introduction to the photogrammetric replication of rock joint surfaces, Chapter 2 introduces the theoretical background involved in photogrammetric digitalization and modelling, Chapter 3 elaborates the research methods applied for the thesis, Chapter 4 introduces the photogrammetric replication of rock joint surfaces methodology as applied in the KARMO research project, Chapter 5 presents the results from the research conducted for the thesis, Chapter 6 introduces some thoughts and discussion based on the findings on the thesis work, and Chapter 7 concludes the thesis and summarizes the findings.

2 Theoretical background of photogrammetry

2.1 Photogrammetry

2.1.1 Introduction

Photogrammetry is a technique for capturing information about object size, shape and position without the need of measuring the object itself, although modelling the object in real-scale does require some reference measures, or known shooting distance. With machine vision algorithms and concepts, photogrammetric process enables us to automatically identify and match image features to be transformed into three dimensional features in object space. (Atkinson, 2001) Photogrammetry aims primarily to reconstruct an object in digital form as a three dimensional object. Reducing three-dimensional object into a two-dimensional image involves loss of information. For example, object areas which are not visible in the image cannot be reconstructed from it. In addition to hidden parts, the lost information includes regions which cannot be recognized due to lack of contrast, limiting grain size or limitations of Depth of Field (DoF), such as induced blurring, for example regions in near front and back of Figure 1 are blurred, which makes capturing of accurate information from these regions difficult, information can be gathered, but the potential errors in modelling do inflate.

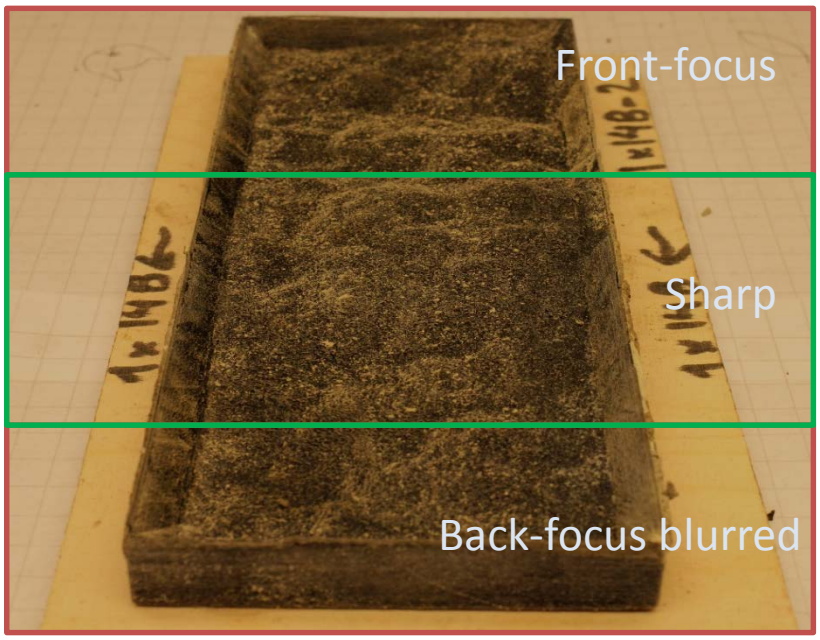

Figure 1. Photogrammetric image of replica mold from KARMO research project.

An image is reduced to define information by two spatial coordinates while in reality the information is stored with three spatial coordinates. This causes geometric changes caused by shape of imaged object, relative positioning of camera and object and defect of optical lenses. There are also changes in color due to reflected electromagnetic radiation recorded in the image being effected by the transmission media and the light-sensitive recording medium. (Luhmann, 2006)

The optical process that creates an image includes light sources, surface properties of the object, transmission media, sensor and camera technology, image processing and further processing. To identify an object from an image by its form, brightness or color distribution, certain methods of image interpretation and measurement are required to obtain radiometric and geometric data of the image. These measurements and mathematical transformations enable the object to be finally modelled. How the reconstructed model corresponds to imaged object depends greatly on the physical and mathematical models used and human knowledge, experience and skill play applied (Luhmann, 2006). The field of photogrammetry handled in this thesis concerns field known as close range photogrammetry applied to multiple imaging. Atkinson (2001) defines close range photogrammetry as a technique where the target object to be measured extends less than 100 meters and cameras are positioned close to it. Photogrammetry in KARMO project is applied with only a few meter distance from the target object. This definition of close range photogrammetry shows that the photogrammetric process applied in KARMO is in some extent an unusual application of that field of photogrammetry in terms of photographing distance to the object of interest and the optical instrumentation applied.

In photogrammetry, shape and object position are defined by reconstructing bundles of rays so that each image point with corresponding perspective center specify the spatial direction of the ray to the corresponding object point. When imaging geometry and location of imaging system are known, every image ray can be defined in 3D space. With use of multiple images and intersecting, corresponding, spatially separated image rays an object point can be located in three dimensional coordinate system. (Luhmann, 2006). Object reconstruction is illustrated in Figure 2.

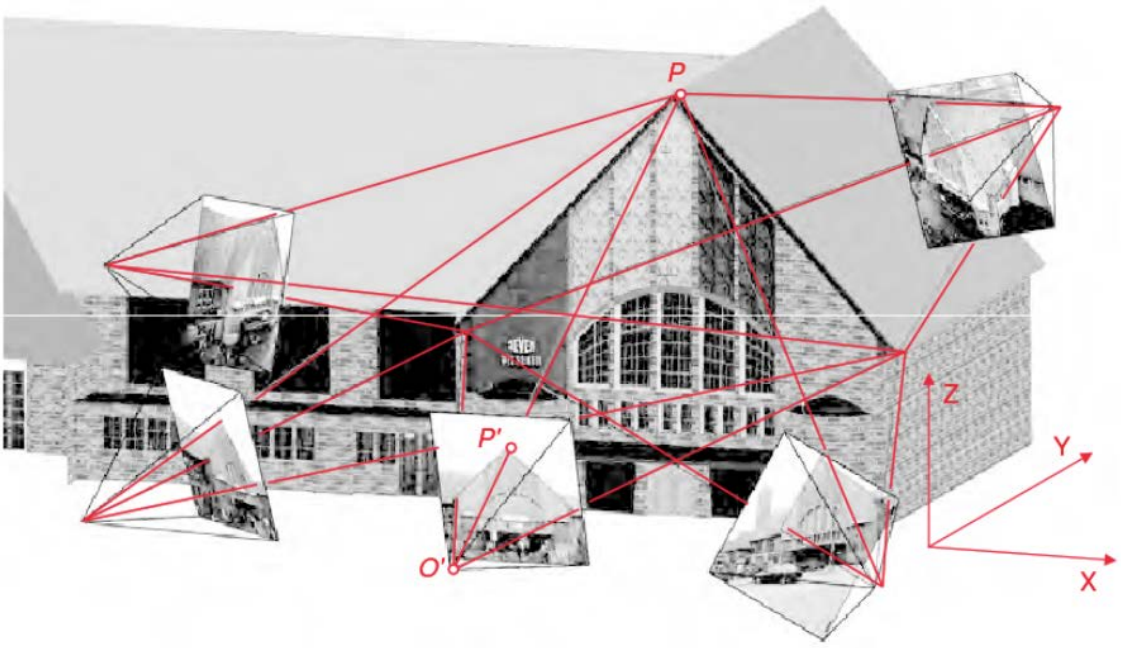

Figure 2. Object reconstruction illustration according to Luhmann 2006

An essential property of photogrammetric image is the scale between object distance and principal distance of the imaging system (Figure 3). The photo-scale with the photogrammetric measurement accuracy are key elements in defining real measurement error associated with the image. With complex objects this error will vary in the image and to access the error in efficient way average error is often handled. (Luhmann, 2006)

Fryer (2007) describes photogrammetric measuring process with following stages: photography, image formatting, image processing, image coordinate measurement, processing and output. Photography depends largely on camera selection, but it should be noted that special cameras designed for photogrammetry are mostly not required. In general, better image quality results in more precise results. Image formatting is often required as images need to be converted to a format suitable for upcoming processing. Image coordinate measurements are needed by model reconstruction algorithms and are often achieved by some automated method. Processing comprises e.g. from image matching or other processing process that forms the output model by use of photographs and spatial properties derived from these photographs.

2.1.2 Single image configuration

Central perspective projection defines a starting point for close range photogrammetry. Central perspective projection is illustrated in Figure 3. A point (P) from three

dimensional object is projected on a projection plane (P') by a line that goes through a perspective centre (O*).* Orthogonal to the projection plane is a perspective axis (XOx'). Perspective axis intersects projection plane principal point (x'). The distance Ox', usually denoted by *c* is the principal distance. This configuration is represented by two three dimensional Cartesian coordinate systems to derive functional relationships between position of an object point (P) and the position of the projection point (P'). First coordinate system (XYZ) is located arbitrarily in object space, while the second system (xyz) has its origin at perspective centre (O) with z-axis directed away from the plane of projection. In the first system (XYZ) the coordinates of the perspective centre (O) are (X_o, Y_o, Z_o) and the coordinates of a point (P) are (X_P, Y_P, Z_P) while coordinates for a point in the second system are ($x_{P'}$, $y_{P'}$, -c). (Robson, 1996)

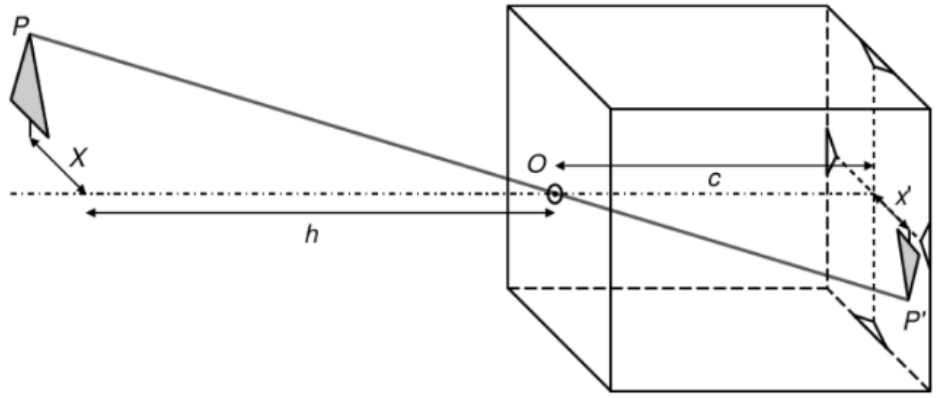

Figure 3. The Perspective Centre by Luhmann (2006)

Vectors relative to coordinate system of object space can be written,

$$X_P = X_0 - uR^t x_{P\prime}, \tag{1}$$

Or in matrix notation,

$$\begin{bmatrix} X_P \\ Y_P \\ Z_P \end{bmatrix} = \begin{bmatrix} X_0 \\ Y_0 \\ Z_0 \end{bmatrix} - u \begin{bmatrix} r_{11} & r_{21} & r_{31} \\ r_{12} & r_{22} & r_{32} \\ r_{13} & r_{23} & r_{33} \end{bmatrix} \begin{bmatrix} x_{P\prime} \\ y_{P\prime} \\ -c \end{bmatrix}. \tag{2}$$

With notations according to previous paragraph, where u is a scalar and the elements r_{ij} define a rotation matrix. With perspective centre, direction of the perspective axis and the principal distance known, there are no single solution for (X_P, Y_P, Z_P). By applying reverse transformation,

$$x_{P'} = u^{-1} R(X_0 - X_P). \quad (3)$$

Or in matrix notation,

$$\begin{bmatrix} x_{P'} \\ y_{P'} \\ -c \end{bmatrix} = u^{-1} \begin{bmatrix} r_{11} & r_{21} & r_{31} \\ r_{12} & r_{22} & r_{32} \\ r_{13} & r_{23} & r_{33} \end{bmatrix} \begin{bmatrix} X_0 - X_P \\ Y_0 - Y_P \\ Z_0 - Z_P \end{bmatrix}. \quad (4)$$

The third equation of *(4)* can be written open for u^{-1} to derive collinearity equations,

$$x_{P'} = \frac{-c[r_{11}(X_0 - X_P) + r_{12}(Y_0 - Y_P) + r_{13}(Z_0 - Z_P)]}{[r_{31}(X_0 - X_P) + r_{32}(Y_0 - Y_P) + r_{33}(Z_0 - Z_P)]}, \quad (5)$$

$$y_{P'} = \frac{-c[r_{21}(X_0 - X_P) + r_{22}(Y_0 - Y_P) + r_{23}(Z_0 - Z_P)]}{[r_{31}(X_0 - X_P) + r_{32}(Y_0 - Y_P) + r_{33}(Z_0 - Z_P)]}, \quad (6)$$

Equations *(5)* and *(6)* can be derived from collinearity of point P, perspective centre (O) and perspective projection of *P -> P'*. These equations offer a base theory for solving coordinates for digital three dimensional model for a real 3D object. (Atkinson, 2001)

There will be two equations for each image point; one for $x_{p'}$ and one for $y_{p'}$. This results in great number of equations (n x m x 2) for a setup with multiple images (n) and image points (m). (Fryer, 2007) In numerous photogrammetric calculations, more observations or known values are available than required for a solution, which results in the fact that no unique solution is available for such system. These systems can be solved with functional or stochastic models. (Luhmann, 2006)

2.1.3 Adjusting multiple images

Various adjustment techniques exists and can be applied in photogrammetric process *(*e.g. Wolf, 1997; Cross, 1990; Mikhail, 1976; Mikhail & Gracie 1981*)*. In most common approaches, equations (5) and (6) are linearized, usually with Taylor's expansion or direct linear transformation (DLT) to allow the use of least square estimation (LSE) (Fryer, 2007).

Each image provides a bundle of rays that are defined by the imaged points and the perspective center. When bundles of rays from multiple images are intersected, a dense network with a potential for high geometric strength can be created. With this method

any number of images can be simultaneously oriented and associated three dimensional object locations calculated. (Luhmann, 2006)

There is random noise on image observations and possibly some systematic errors involved as well, so the corresponding image rays between images do not necessarily intersect at same point. This leads to a problem where the best fit is to be solved for the 3D point location. Point coordinates are solved by minimizing the weighted squared sum of observation errors for the image space. The adjustment allows solving image orientation in the same way as well. This configuration leads to a problem of finding the best fit for bundle of image rays with respect to each other and known object points. (Heikkinen, 2005) This estimation is called bundle adjustment (Brown, 1976). Bundle estimation makes it possible to assess the accuracy of the resulting points without any exterior data.

2.1.4 Bundle Adjustment

Essentially bundle adjustment is a parameter estimation problem for which choosing a method for quantifying total prediction error with model, parametrized by combined scene and camera parameters, gives access to measure for model fitting. Nonlinear least squares is one of the most basic parameter estimation methods, but the main problem with least squares is its high sensitivity to outliers. Outliers can be detected and accessed by tracking down observations affected by blunders such as correspondence errors. This model applies to both; geometric and intensity-based matching of image patches. Defining a model for quality metric allows optimization of this model. In essence this means minimizing chosen function over defined parameters for applied quality measure. (Triggs et al. 1999). Applicable optimization methods are further discussed elsewhere e.g. (Flecher, 1987*;* Nocedal & Wright, 1999*;* Gill et al. 1981). Triggs et al. (1999) recommend using second order Gauss-Newton method with sparse factoring of the Hessian for optimization of batch problems, unless the problem is very large, in which case iterative linear solver like Conjugate Gradient or Limited Memory Quasi-Newton should be considered.

Traditionally the applied mathematical models result in a three dimensional point clouds which are then processed to digital terrain models (DTM), digital elevation models (DEM) or other digital formats to represent a surface in terms elevation (z) for series of

(x,y)-coordinates. (Frayer, 2007) Joint surface replication and discontinuity roughness evaluation routines generally produce triangular irregular network (TIN) surfaces, mostly in binary or ASCII stereolithography (.STL) format. Point cloud to surface transformation is traditionally achieved with triangulation process, e.g. Delaunay triangulation.

The bundle adjustment method applied in KARMO research project is a multicore bundle adjustment, an inexact Newton type bundle adjustment algorithm exploiting hardware parallelism, implemented in the VisualSFM –software. The algorithm is argued to provide great savings in runtime and thus be very efficient in solving large scale 3D scene reconstruction problems (Wu et al. 2011).

2.1.5 Structure from Motion

In comparison to traditional bundle adjustment methods, camera pose and scene geometry can be solved simultaneously and automatically using a highly redundant bundle adjustment based on matching features in multiple overlapping, offset images. This method is called Structure from Motion (SFM). SFM methodology first identifies features from images, which are then matched by using non-linear least-squares minimization.

A popular solution for feature identification is the Scale Invariant Feature Transform (SIFT) object recognition system. (Westoby et al. 2012) SIFT algorithm (Lowe, 1999) searches and combines non-scale-dependent image features by transforming image to a collection of local feature-vectors, so called SIFT-keys, which are saved to a database. Images are then gone through by comparing image features to these SIFT-keys, and matched accordingly. (Lowe, 1999) These features are invariant to image scaling and rotation, and partially invariant to changes in illumination conditions and 3D camera viewpoint (Lowe, 2004).

Westoby et al. (2012) present that, changes in complexity, lighting and materials in individual scenes influence the image texture, and makes it impossible to define minimum number of photographs necessary for accurate scene reconstruction, and further recommend obtaining as many images as feasibly possible. The KARMO project aims to test stated impossibility, and evaluate its applicability. The general view is that there should be a saturation point for model creation where the achievable point

density would saturate with certain number of image. This effect is further examined in chapter 5.3.

Westoby et al. (2012) describe an example method for 3D scene reconstruction, in which feature matching is performed with sparse bundle adjustment, which is to gather information about camera pose and extract a low-density point cloud. In this method features from multiple images are matched with approximate nearest neighbor (Arya et al. 1998) together with Random Sample Consensus (Fischler & Bolles, 1986). Which leads to formation of connections between identified features and sets of pictures. Connections with at least two identified features and three images are used for point-cloud reconstruction and connections that do not meet these requirements are discarded. Correspondences of identified features form constraints on camera pose orientation, which can be reconstructed with similarity transformation, while error minimization can be achieved using a non-linear least-squares solution (Szeliski & Kang, 1994; Nocedal & Wright, 1999).

Sparse point-cloud produced by bundle adjustment can be enhanced by creating a density point-cloud with implementation of Clustering View for Multi-view Stereo (CVMS) (Furukawa & Ponce, 2007; Furukawa, 2010) and Patch-based Multi-view Stereo (PMVS) algorithms (Furukawa, 2007). These algorithms apply camera positions derived from sparse bundle adjustment to decompose overlapping images into subsets with CMVS. PVMS in the other hand is used to reconstruct 3D data from retrieved clusters (Furukawa, 2007). The PVMS processing step increases point density considerably (Westoby et al. 2012).

2.2 Quality of digital model

2.2.1 Theory

Fryer (2007) lists error sources applicable in photogrammetric process, and further underlines that computed results cannot be perfect. Fryer (2007) divides errors in three groups; measurement errors, systematically occurring errors and genuine mistakes or "gross errors". Measurement errors affect image coordinates and coordinates of control points. Measurement errors are randomly distributed and can be positive or negative. Systematically occurring errors are caused by imperfections in fixed values in calculations or by errors in the assumed geometry of the collinearity equations. Systematically occurring errors can occur for example from errors in pixel geometry of digital sensor, lens distortion or non-perpendicularity between the sensor plane and the lens axis. Genuine errors in measurements or processing include wrongly identified and measured control points, falsely matched points during automated measurement or errors conducted by operator, such as using wrong units for calculation parameters.

Quality of results from photogrammetric process can be accessed by precision, accuracy and reliability (Atkinson, 2001). In this work precision describes the variability of quantity, accuracy defines the difference between calculated quantity and true value and reliability describes quantity properties such as precision of the measured coordinates from the image, the angels between intersecting rays and precision of control point coordinates and compares these parameters to theoretical reference.

Meeting accuracy requirements set for a project is generally of highest priority in practical photogrammetric project planning. Measurement accuracy depends on stability and calibration of the camera, the accuracy of image processing system and quality of feature identification, which require balancing according to priorities set in the planning process. (Luhmann, 2006). Luhmann (2006) emphasizes the importance of objective selection in planning of photogrammetric process, as the objective defines the quality of image acquisition and processing, as well as image scale and configuration. Close range photogrammetry bases on LSE process, which enables the use of several indicators of the quality of measured and derived data to be used for assessment for the quality of data after the measurement, and for assessment for a measuring of system meeting specific requirements (Atkinson, 2001).

2.2.2 In practice

Accessing recorded surface models suitability to experimental requirements requires evaluation of overall performance of recording environment. Overall performance can be evaluated with characterization of model quality in terms of global measure of error. According to Cooper & Cross (1988), accuracy of the model can be estimated with evaluating applicability of functional model and can be accessed with evaluation of lens distortion model. Precision describes random errors between repeated measurements in the same conditions, and cannot be eliminated with applying corrections (Cooper & Cross, 1988). Precision can be evaluated trough estimation of global precision, which can be computed using the standard deviation of errors. The root mean square error quantifies random and systematic errors together in a normal approach (Butler et al. 1998; Chandler et al. 2003; Luhmann, 2006). Gross errors can be assessed by comparison of DEMs using different baselines (Butler et al. 1998), or by extracting values of interest from different imagery (Brasington et al. 2003). With error assessment, the difficulty rises from challenges in defining reference values for parameters of interest (Lane et al. 2000).

In practice, topographic data quality is analyzed by comparison of small number of check points for a digital model over the measured surface (Bertin et al. 2014). Bertin et al. (2014) presents that alternative measuring devices are usually used for location checking within the digital model. Limitations for this type of approach include errors of positioning, low density and arbitrary distributions for points of interest. An example of this approach is to apply laser scanning with photogrammetry. While laser scanning can be very accurate in theory, it is not error-free in practice (Hodge et al. 2009). Therefore model reconstruction is required together with error editing.

Alternative approach for evaluation of quality of digital model is to measure objects of known size (Bertin et al. 2014). Both techniques have their complications, so quality assessment for an application of photogrammetry requires approach that is defined for that particular method. The applied practical measurement technique was selected as comparing surface roughness in different phases of replication with hand measured roughness metrics.

3 Research Methods

3.1 Initial data

Photographic replication process conducted in KARMO research project provided initial data applied for studies conducted in this thesis. First, original rock slab was photographed and processed with photographic process presented in chapter 3.2 Then, produced 3D surface was inverted to an inversion model for a casting mold that was printed with a 3D printer. Printed mold was then processed with the photogrammetric process presented in chapter 3.3 to produce a point cloud and a digital surface model following the same modelling practices as applied for the original rock slab. Finally, surface replicas were casted and processed with the photogrammetric process presented in chapter 3.3 resulting in point clouds and surface data from the replicas.

Originally produced data was further enhanced by additional photogrammetric modelling. The original rock slab was photographed with over 1000 photographs to further analyze the accuracy of applied photogrammetric modelling procedure. The rock slab was also photographed with same imaging configuration as applied for the casting molds and replica samples. Finally the original rock slab was modelled by applying an alternative photogrammetric process. Alternative photogrammetric process for original rock slab was performed with Artec™ EVA 3D scanner, to produce comparable reference point cloud and surface model for analysis of digital model quality.

The initial data contain polygon file formatted (.PLY) point clouds of the original rock slab, casting molds and final replica samples, which were further triangulated to STL formatted TIN surfaces and saved in ASCII text format.

3.2 Evaluating roughness

3.2.1 Characterization of discontinuity roughness

2D roughness evaluation

A range of different parameters for characterization of discontinuity roughness exist. This thesis focuses on evaluation of joint roughness coefficient (JRC) from empirical approaches by analyzing hand measured profilometry and two statistical approaches for deriving JRC metrics from digital models of a surface, presented in the following paragraphs.

Joint roughness coefficient

Conventional roughness parameterization is conducted with linear profiling that requires direct contact with the surface and results in the JRC parametrization, derived from empirical studies (ISRM, 1979). Barton-Bandis empirical shear criteria (Barton & Bandis 1990) estimates shear strength τ of an unfilled, un-weathered rock discontinuity,

$$\tau = \sigma_n \tan\left[\phi_b + JRC \log_{10}\left(\frac{JCS}{\sigma_n}\right)\right], \quad (7)$$

where σ_n is the applied normal stress, ϕ_b is the basic friction angle, JRC is the Joint Roughness Coefficient describing the roughness of the surface and JCS is the Joint wall Compressive Strength describing intact strength of asperities.

The JRC parameter is essentially a curve fitting parameter ranging from 0, for very smooth surfaces, to 20 for rough surfaces. Barton and Choubey (1977) developed a series of standard profiles to allow visual comparison of roughness profile of the surface to these standardized profiles. The standard profiles allow JRC parametrization to be conducted in rapid succession. However, manual measurements are subjective and can lead to overestimation (Grasselli & Eggar 2003). Barton and Bandis (1982) expanded selection for practical parametrization by developing a method for deriving JRC from maximum asperity altitude. The standard JRC profiles are presented in appendix 1, and the tables for determining JRC with amplitude method is presented in appendix 2.

Subjectivity of JRC characterization is an issue that has been tangled by numerous researchers, and empirical correlations have been searched with various statistical and fractal approaches (Myers, 1962; El-Soudani, 1978; Malinverno, 1990; Lanaro, 2000; Fardin et al. 2001). The statistical approaches selected for inspections in this thesis are presented in the following paragraphs.

Statistical approaches

Several recently emerged techniques applying optical instruments offer an alternative ways for quick discontinuity measurements in both laboratory and in situ environments without the need for direct contact (Grasselli et al. 2002; Haneberg 2008; Rahman et al. 2006; Baker et al. 2008). Applications of these techniques have evaluated discontinuity roughness with statistical approaches describing the amplitude of roughness and the texture of discontinuity surface. These studies have characterized discontinuity roughness with various mathematical approaches and the methods used for roughness evaluation in this thesis are limited to; determining surface lengths along profiles (Maerz et al. 1990) and root mean square characterization of local slopes (Tse & Cruden, 1979).

Surface length measurement proposed by Maerz et al. (1990) bases on empirical correlation of JRC and Roughness Coefficient (R_p). R_p is defined as the ratio of the true profile length L_t to the nominal profile length L_n,

$$R_p = \frac{L_t}{L_n} = \frac{\sum_{i=1}^{N-1}\sqrt{(x_{i+1}-x_i)^2+(y_{i+1}-y_i)^2}}{L_n}, \qquad (8)$$

where (x_i, y_i) and (x_{i+1}, y_{i+1}) represent coordinates for a point from a 2D profile and N represents the total number of points in the line profile (El-Soudani 1978). Maerz et al. (1990) present an empirical correlation in the form of,

$$JRC = c\,(R_p - 1), \qquad (10)$$

where JRC is expressed in terms of a constant c, varying from 400 to 411, and the Roughness Coefficient minus one.

Slope measurement proposed by Tse and Cruden (1979) is the root mean square (RMS) estimate from the local slopes of the profile with intervals between measured data points. Relationship with JRC and RMS can be represented with,

$$JRC = 32.2 + 32.47 \log(Z_2), \quad (11)$$

Where Z_2 represents the RMS,

$$Z_2 = \sqrt{\frac{\sum_i^{N-1}(z_i - z_{i+1})^2}{(N-1)ds^2}}, \quad (12)$$

where z is the height of the profile above reference line, N the quantity of measures and ds the distance between measures.

The values of Z_2 and R_p are sensitive to sampling interval used to digitalize the profiles (Yu & Vayssade, 1991). Thus, the use of these equations for JRC estimation requires a sampling window that is consistent with the sampling window used for originally developing these equations.

Limitations of conventional roughness estimation

Traditional discontinuity roughness evaluation results in two dimensional parametrization of the surface, which can be extended in some cases to a three dimensional study. These methods have some limits that have been acknowledged, for example Tatone (2009) summarizes these limits to:

- Empirical methods are subjective to practitioner conducting parametrization.
- Most approaches consider 2D profiles only.
- Methods are non-directional, and cannot describe anisotropy in roughness that is known to exist.
- All statistical and fractal methods depend on measurement quality, and can be highly effected by resolution and noise of the surface measurements.

To counter these limitations, Tatone and Grasselli (2009) developed a method for evaluation of three-dimensional roughness of fracture surfaces in brittle geomaterials, which is described in the following chapter.

3D roughness evaluation

Tatone and Grasselli (2009) present a method for three-dimensional roughness characterization. The paper aims to propose a standard methodology for 3D roughness characterization for a surface topography. The authors argue that formerly dominating analysis of 2D roughness profiles based on necessity with lack of tools with sufficient accuracy, resolution and ease of use to be used for characterization of a 3D surface topography. As this restriction has been lifted with new generation of measurement techniques, applying variety of optical instruments, it was possible to collect a 3D point cloud, able to form a highly detailed digital model of the surface, to be used for further analysis in 3D space. These optical instruments include laser scanners (Chae et al. 2004; Fardin et al. 2004), close-range photogrammetry (Haneberg, 2007; Lee & Ahn, 2004; Baker et al. 2008), and stereotopometric scanners (Hong et al. 2006; Grasselli et al. 2002; Nasseri et al. 2009).

Tatone and Grasselli (2009) present that the surface area damaged on a laboratory shear test is strictly related to the surface topography and is typically restricted to the asperities having an opposite local dip orientation to the shearing direction (Grasselli et al. 2002; Gentier et al. 2000), and primarily develop in the areas with steepest asperity faces (Grasselli et al. 2002; Gentier et al. 2000; Haberfield & Johnston, 1994; Yang & Chiang, 2000; Seidel & Haberfield, 2002). This reasoning suggest that a roughness parameter for a surface should be based on the distribution of the asperity angles with respect to shearing direction.

The methodology for 3D roughness characterization according to Tatone and Grasselli (2009) can be presented with four steps. The first step is the acquisition of the 3D surface, typically in the form of a point cloud. The second step is preprocessing the surface topography to a TIN surface for further analysis. The third step is to align the triangulated surface with respect to the original surface. The fourth and final step is to analyze the triangulated surface with respect to orientation and steepness of the surface asperities.

For roughness evaluation in an analyzing direction (t), the orientation of each triangle, forming the rough surface, can be represented with triangle dip (θ) and azimuth (α). The dip is defined as the maximum angle between the best-fit plane and the analyzed

triangle, and the azimuth is defined as the angle between the selected analysis direction and the projection of the true dip vector (d) on to the best-fit plane. The analysis parameter of apparent dip angle (θ^*) can be obtained by projecting the true dip vector (d) onto a vertical plane along the analysis direction (t). (Tatone & Grasselli, 2009) The geometric triangular definition is illustrated in Figure 4.

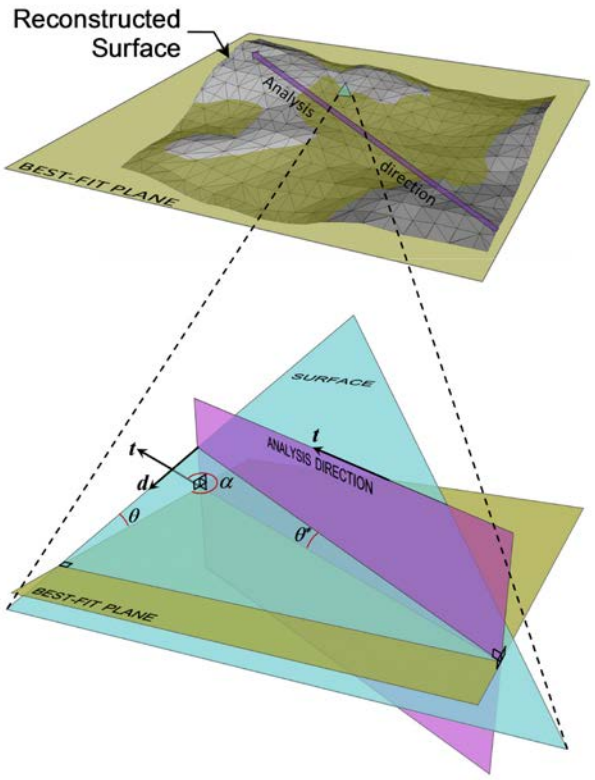

Figure 4. Schematic diagram for the definition of azimuth, dip and apparent dip in relation to the selected analysis direction, presented according to Tatone and Grasselli (2009).

For the apparent dip angles for each triangle it is possible to define the fraction of the surface that is more steeply inclined that progressively grater threshold values of (θ^*). This fractional are is referred in the 3D roughness analysis as the normalized area (A_{θ^*}). The A_{θ^*} is defined by the area of the surface that has an apparent dip greater than the selected threshold value normalized with respect to the total area of the surface. The analysis process is considered analogous to the sieve analysis, by the authors. Considering the analysis represents only one analysis direction, the process must be repeated to characterize the aerial distributions in other directions. (Tatone & Grasselli, 2009).

Assuming that the proportion of steeply dipping asperities is directly related to the roughness of the surface, the relative roughness of surfaces can be objectively evaluated by comparing the cumulative distributions of A_{θ^*}(Tatone & Grasselli, 2009). The relationship between the $A_{\theta^*}$and θ^* can be represented by,

$$A_{\theta^*} = A_0 \left(\frac{\theta^*_{max} - \theta^*}{\theta^*_{max}}\right)^C, \quad (13)$$

where A_0 represents the normalized area of the surface corresponding to an angular threshold of θ^* in the chosen direction, θ^*_{max} is the maximum apparent dip angle of the surface in the chosen analysis direction, and C is a dimensionless fitting parameter, calculated by nonlinear least-squares regression analysis, characterizing the shape of the distribution. (Grasselli et al. 2002; Grasselli, 2006)

A value of C equals 0 characterizes a saw tooth profile where all asperity faces have the same dip angle, and a value of C approaching zero characterizes a smooth profile. This leads to an inspection where C provides an objective measure of surface roughness in an analysis direction. Still the value of C alone is not adequate to define the roughness completely. (Tatone Grasselli, 2009)

Grasselli et al. (2002) inspected C as the measure of surface roughness, with direct shear tests, and found out that C does not correlate well with observed degree of roughness. However, a strong correlation was found between θ^*_{max}/C and corresponding shear strength for tested discontinuity specimen. (Grasselli et al. 2002) Tatone and Grasselli (2009) reevaluated the inspected the empirical correlation in an attempt to find physical bases for the relationship. This evaluation lead to a discovery of significant relation between the values of θ^*_{max}/c and area under the corresponding best-fit curves given by equation (13). The areas under the curve represents the proportion of steeply dipping asperities and, thus, relative roughness. The integral for equation (13) from θ to θ^*_{max},

$$A_0 \int_0^{\theta^*_{max}} \left(\frac{\theta^*_{max} - \theta^*}{\theta^*_{max}}\right)^C d\theta^* = -A_0 \left(\frac{\theta^*_{max}}{C+1}\right) \times \left(1 - \frac{\theta^*}{\theta^*_{max}}\right)^{C+1} \Big|_0^{\theta^*_{max}} = A_0 \left(\frac{\theta^*_{max}}{C+1}\right), \quad (14)$$

where A_0 is the normalized surface area steeper than θ^o ni the analysis direction, and the term $\theta^*_{max}/(C+1)$ characterizes the mean apparent dip angle of the surface in the analysis direction, represents the area under the curve. (Tatone & Grasselli, 2009)

Tatone and Grasselli (2009) conclude that the parameter $\theta^*_{max}/(C+1)$ is very similar to the original empirical parameter, and is thus proposed to be evaluated as the metric of surface roughness. The behavior of this metric for C from zero to infinity, ranges from zero for smooth surface, to θ^*_{max} for a saw tooth surface. Furthermore, it should be emphasized that although A_0 was inspected to be nearly constant at 0.5 in the experiments conducted by Tatone and Grasselli, this is not true for all fracture surfaces; in some cases A_0 could vary significantly in different directions, in these cases it is proposed to use $2A_0[\theta^*_{max}/(C+1)]$ as a roughness metric. (Tatone & Grasselli, 2009).

The presented 3D roughness characterization technique is demonstrated with measurement data, collected with Advanced TOpometric Scanner (ATOS), which consists of points on a roughly 250 um xy grid over a nominal area of 150 * 150 mm2, but is argued to be independent on the measurement system. (Tatone & Grasselli, 2009) In comparison, the photogrammetric measurement technique applied in KARMO, presented by Uotinen et al. (2015) is reported to achieve point density of 16.2 points / mm2, which corresponds roughly to points on a 250 um xy grid over a nominal are of 1700 * 600 mm2. The photogrammetric measurement technique of KARMO has been able to further enhance the point density up to 42.8 points / mm2, corresponding roughly to points on a 155 um xy grid over a nominal are of 170 * 60 mm2 (Kallio, 2015).

Roughness evaluation methods implemented in this thesis are:

- Hand measured JRC measurements with a hand held profilometer,
- JRC measurements derived from the digital models with slope length and surface length –methods,
- 3D roughness evaluation with surface area method derived from 2D surface length method, and
- Directional 3D roughness evaluation introduced by Tatone and Grasselli (2009).

Roughness evaluation is conducted for original rock slab, casting mold and final replica sample, produced in the KARMO I. And for digital models of rock slab, casting mold and replica sample produced with photogrammetric modelling process presented in chapter 4.3, produced in KARMO II.

3.2.2 Data preparation

Digital surface models were prepared for discontinuity roughness evaluation by performing a preparation MATLAB routine. Preparation routine defines a reference coordinate system for the TIN surface by fitting a best fit plane for surface points and setting orthogonal base vectors as coordinate system. Best fit plane and base vectors are illustrated in Figure 5.

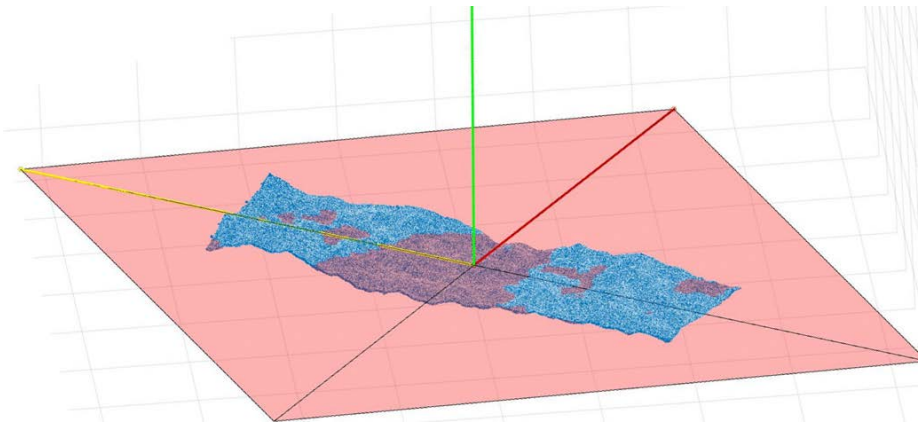

Figure 5. Point cloud from TIN surface with Best Fit Plane, plane normal and base vectors

Applied routine then defines sectioning plane along shearing direction of the surface by taking a dot product from the plane normal and base vector in shearing direction. Sectioning plane is illustrated in Figure 6. Then the routine searches for point pairs that define triangulation triangles and lists these points to define lines for triangle intersection search. Finally line intersections between triangulation lines and sectioning plane are calculated from line and sectioning plane equations, and intersection points are gathered for 2D section creation.

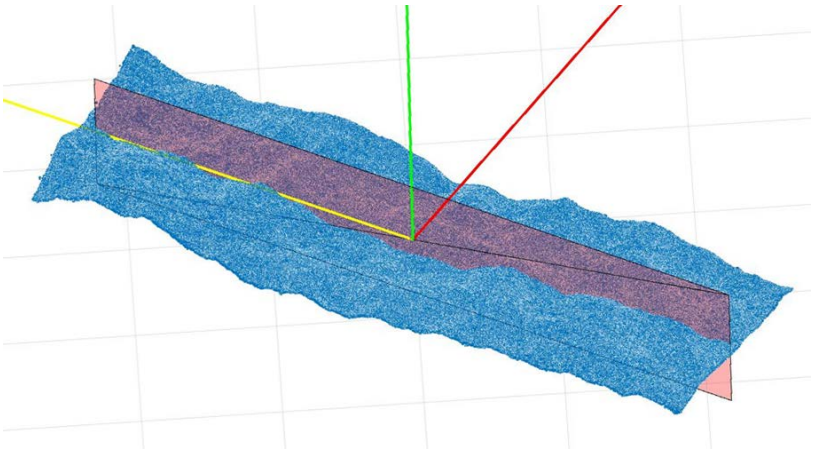

Figure 6. TIN surface, sectioning plane in shearing direction and normal vectors to Best Fit Plane

Created point list is then sorted for data analysis purposes. First, defining of 2D coordinates (x,y) for points is performed by distance from a plane perpendicular to sectioning plane far from point cloud (x) and distance from offset of original plane that is projected away from point cloud neighborhood (y). Distances from these planes are calculated by taking an orthogonal projection,

$$Proj_L(\bar{x}) = \frac{\bar{x}\cdot\bar{v}}{\bar{v}\cdot\bar{v}}\bar{v}, \tag{15}$$

of a vector from plane to the point to the plane of interest and defining distance from plane (z) to be subtraction of projection vector (yh) from point vector (y),

$$yh = \frac{\bar{x}\cdot\bar{n}}{\bar{n}\cdot\bar{n}}\bar{n} + \frac{\bar{x}\cdot\bar{y}}{\bar{y}\cdot\bar{y}}\bar{y}. \tag{16}$$

Finally, point list is sorted according to distance from plane perpendicular to sectioning plane.

3.2.3 Evaluating JRC from TIN surface

Implementation

Data preparation results in two dimensional section profile from the original TIN surface. The evaluated TIN surfaces are sectioned in same pattern as applied in the previous stages of KARMO research project for measurements of JRC and roughness amplitude. Sectioning workflow is presented in the chapter 3.2.2. Samples are split into six sectioning lines, with three lines in shearing direction and three lines perpendicular to it. The sectioning pattern is illustrated in Figure 7.

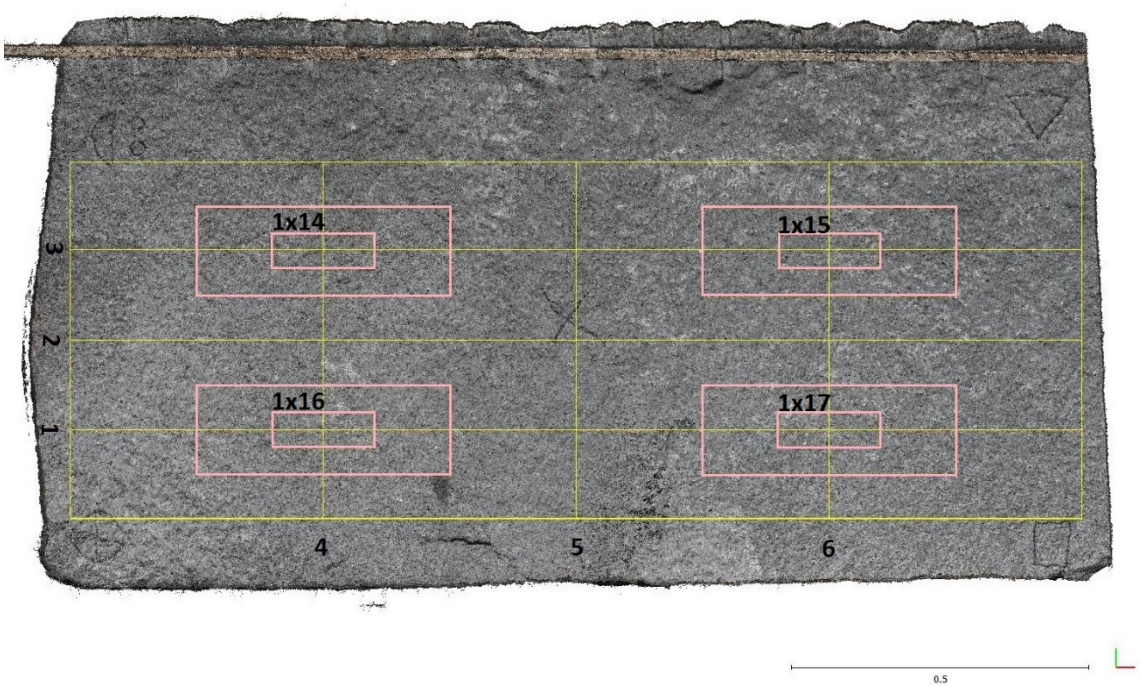

Figure 7. Original rock slab with illustrative sectioning for JRC and amplitude measurements. Yellow grid represents fresh joint surface and trimmed TIN surface, lines 1-6 represent measurement lines, and red lines represents surface areas represented by replicas 1x 14-17. Figure presented according to Kallio (2015).

The two dimensional sectioning profiles are normalized with sampling interval of 0.5 mm to maintain optimal behavior of statistical JRC modelling, as this interval was originally used for derivation of the statistical functions**.** JRC values are calculated with surface length method (Maertz et al. 1990) and slope measurement method (Tse and Cruden, 1979), presented in chapter 3.2.1. Sectioning profiles are sampled with three sampling methods to compare effects of sampling and roughness evaluation with traditional profilometry measurements. Sampling techniques are illustrated in Figure 8.

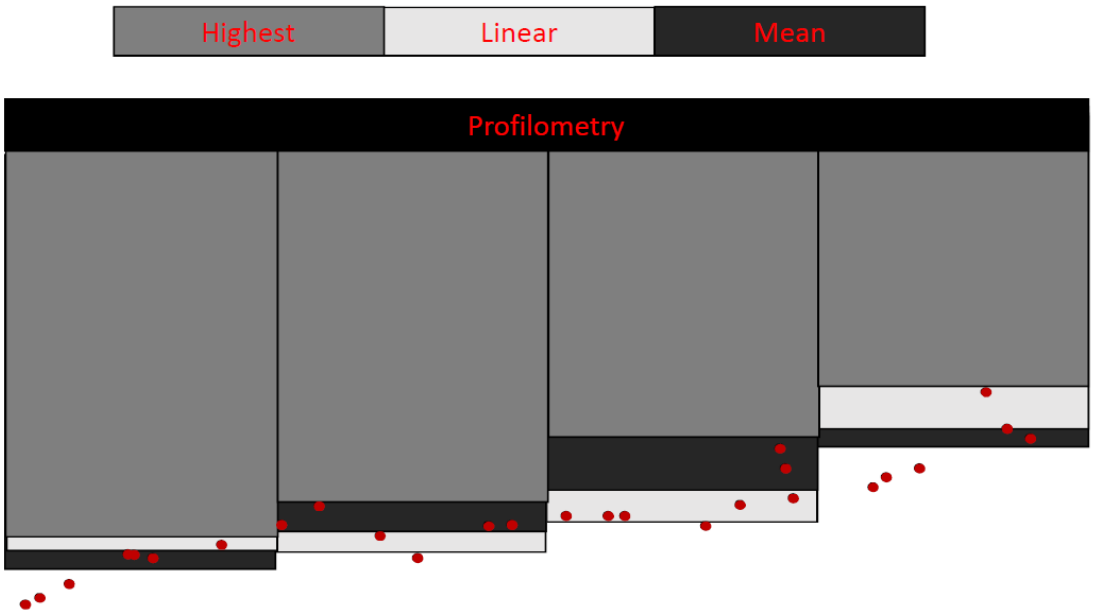

Figure 8. Illustration of sampling methods with a conceptual model

Inspected sampling methods are: Linear, Highest and Mean. Linear sampling derives normalized points by sectioning profiles with chosen sampling interval, and calculating linear interpolation from nearest points in both sides of the sectioning line. Highest sampling chooses the highest point in sampling window to represent height profile similar to hand applied profilometry. Mean sampling selects the mean height of points in sampling windows to represent the sampling window.

4 Photogrammetric replication of rock joint surfaces

4.1 Photographic measurements in practice

Economic aspects and accuracy requirements are generally the factors that define a practical photography project. Accuracy estimates depend primarily on image measurement accuracy, image scale and design factor of the imaging configuration. Image measurement accuracy can be increased with proper calibration of camera and applying a stabile shooting platform, and optimizing image processing system with respect to image quality, measuring algorithm, instrumental precision and feature identification method. These criteria cannot all be optimized together, but a balance between different factors can be reached. (Luhmann, 2006). Perfect configuration for a photogrammetric project cannot be defined unambiguously because it always depends on circumstances of the object.

Atkinson (2001) lists different restrictions applied to imaging configuration; Image scale, Image quality, Object environment, Depth of field, imaging angle, number and distribution of images, intersection angle and viewing angle and visibility. Image scale is affected by object distance, principal distance and usable image format and controls required number of images. Image quality is controlled by applied measurement technique. Object environment sets requirements for required image numbers or to use of additional lenses. Depth of field, controlled by image scale and f-stop, for significant 3D shape and difficult light conditions restricts usable camera stations. Imaging angle is controlled by the surface geometry of object photographed. Number and distribution of image points together with camera stations effect the bundle adjustment functionality. Good intersection angles are critical for the accuracy on point measurements, and optimal ray intersections angles are around 90 to 100 degrees, which corresponds roughly to a shooting angle from 30 to 45 degrees. Viewing angle and visibility define how much of photographed geometry can be captured by the imaging process. (Luhmann, 2006)

4.2 Development of photogrammetric replication of rock joint surfaces

This thesis concentrates on assessing and further developing a photogrammetric replication process developed on KARMO research project. In KARMO I, a granite rock slab, split from larger boulder, was acquired for a source geometry. Approximately 10 cm long wedges were used for the splitting, applied in one side of the boulder with 10-15 cm spacing. The rock slab was also sawn to approximately 3 cm thick plate to produce a smooth surface on the other side of the rock slab. The granite rock surface with geometry of interest was approximately 175 cm x 95 cm. Some damage from frost due to storing arrangements between cutting and photographing were considered possible for the surface. The inflicted damages are presumed to be very small due to storing time for the rock slab being relatively short. The surface was cleaned from dust and dirt as well, prior to photographing. (Uotinen et al. 2015).

The photographing was performed by using a Canon EOS 600D DSLR camera and a Canon EF 35mm f/2 IS USM objective. The rock slab was photographed outdoors in a shady location. The aperture for imaging was set to f/11, exposure time to 1/60 seconds and ISO value to 100. Reference measures were provided with a folding rule that was placed on the edge of the rock. Rock slab was photographed with 414 photos from different angles (Figure 9, Figure 10). Most of the photos were shot from close range with small translation movements and large overlaps. The camera angle varied from 30 to 80 degrees in vertical direction and from -45 to +45 degrees in horizontal direction. Some pictures were taken with different sensor angle varying from 0 to 45 degrees. Some images were taken from longer, up to 4 m, distance to capture the whole slab in a single image. (Uotinen et al. 2015)

Figure 9. Camera positions in photographing of the rock slab, according to Uotinen et al. (2015)

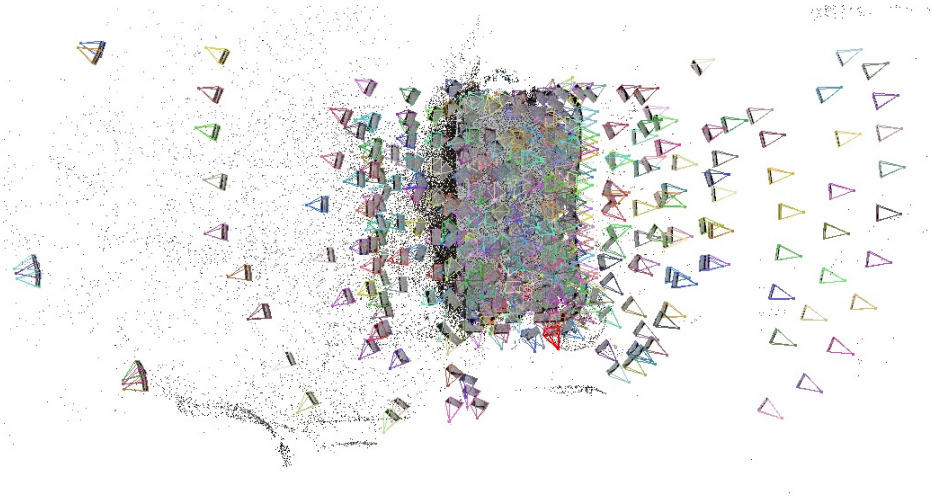

Figure 10. Camera positions in the photographing of the rock slab from above presented, according to Korpi (unpublished)

Photographs were processed to a point cloud with VisualSFM 0.5.25 software. Point cloud was produced with applying first “Open Multi Images” function, then applying “Compute Missing Matches” function, then “Compute 3D reconstruction” function, and finally applying “Run Dense Reconstruction”. (Korpi, unpublished) Original surface and produced point cloud are illustrated in Figure 11.

Figure 11. (Upper) Original rock slab with wedging damages and a reference ruler on the upper right hand side. (Lower) Processed point cloud from VisualSFM routine.

VisualSFM software is an implementation of Structure from Motion routine integrating SiftGPU (Wu, 2007), Multicore Bundle Adjustment (Wu, 2011), incremental Structure from Motion (Wu, 2013) and Clustering Views for Multi-view Stereo (CVMS) (Furukawa, 2010). Feature detection in VisualSFM is achieved with SiftGPU routine, which is an implementation of SIFT (Lowe, 1999) algorithm, that processes image pixels parallel to build Gaussian pyramids and detects Difference of Gaussians (DOG) Keypoints. Then ShiftGPU uses a GPU/CPU mixed method to build keypoint lists, basing on GPU list generation (Ziegler, 2006). Finally SiftGPU processes keypoints parallel to extract keypoint orientations and descriptors. Bundle Adjustment method implemented in VisualSFM is called Multicore Bundle Adjustment, which is a computer vision algorithm that applies Newton type Bundle Adjustment with

exploitation of hardware parallelism for effectively solving large scale 3D scene reconstruction problems. Incremental Structure from Motion (ISFM) routine applied in VisualSFM follows an implementation presented by Wu (2013). This implementation includes a preemptive matching method, which is argued to be able to significantly reduce the feature matching cost for large scale SFM. The practical run time of this particular ISFM-routine is reported to be approximately O*(n)*, order of *n* time complexity, for large problems, while commonly known cost of ISFM is O(n^4) (Wu, 2013). For dense reconstruction, VisualSFM implements a PMVS/CMVS tool chain by Yasutaka Furukawa (Furukawa, 2010). The tool chain takes the ISFM input, and decomposes the input images into a set of image clusters of manageable size, for which a MVS routine can be applied to reconstruct a dense 3D reconstruction. (Wu, 2011) The substantial reduction in computational requirements, achieved with these implementations, strongly supports the use of this routine for photogrammetric replication of rock joint surfaces.

After point cloud processing, the Cloud Compare 2.5.5.2 software was applied to crop out unused parts of the point cloud from outside of the photographed rock and some compromised parts of the rock. These compromised parts included half barrels, cracks and undulation induced by the applied splitting process. Elimination of these regions were conducted to achieve a surface, which would be representative to a natural fresh rock joint. Then information from a reference measure was applied to scale the point cloud to correct size. This procedure resulted in a point density of 16.2 points / mm^2 for the point cloud representing a 1.7 m x 0.6 m rock slab. (Uotinen et al. 2015)

To create a 3D-mesh from the point cloud representing the rock slab, the point cloud was rotated and translated to a 2D plane with principal component analysis (Dimitrov, 2008) and triangulated with 2D-Delaunay triangulation routine that applies Delaunay 2D (best LS plane) method. (Girardeau-Montaut, 2014). Mesh production is illustrated in Figure 12.

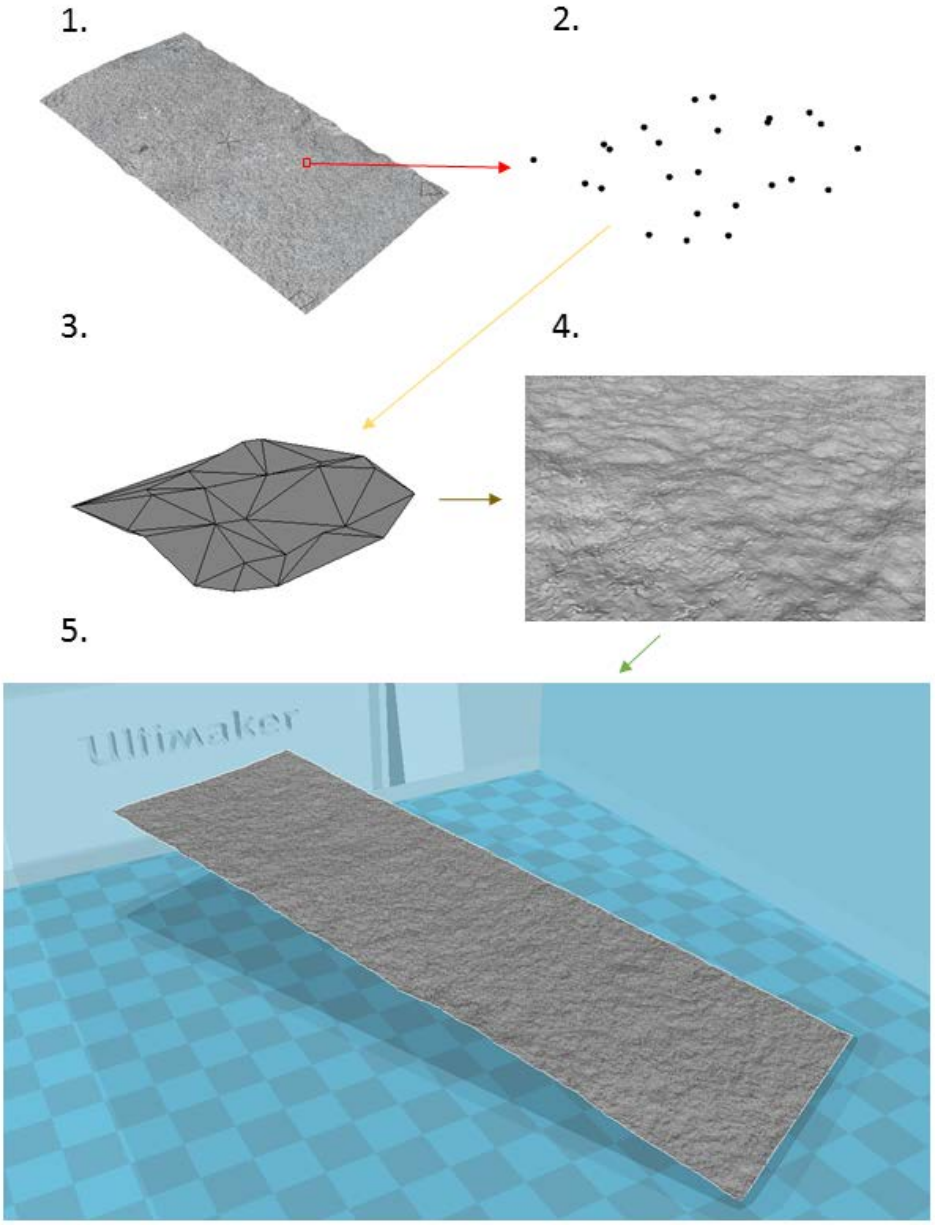

Figure 12. Mesh production principal, original point cloud presented in section 1, zoomed view in section 2, triangulation in section 3, zoom view of final triangulated surface in section 4 and final surface viewed in Cura software in section 5.

Produced 3D mesh was saved in STL ASCII text format. Generating a mesh for geometry sub-categories, which were scaled to a sampling size (170 mm x 60 mm) and sheared in portable shear box, the rock slab geometry was cropped to representative geometry surfaces (10x, 7.5x, 5x, 2.5x and 1x). (Uotinen et al. 2015) The cropping pattern is illustrated in Figure 13.

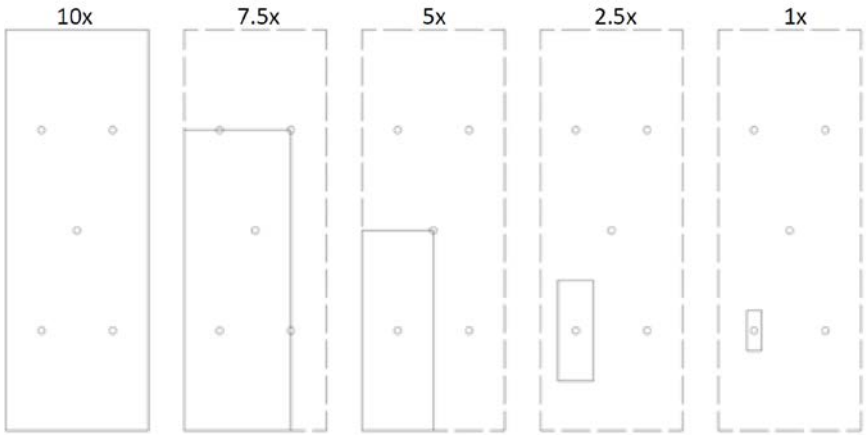

Figure 13. Sub-sampling of the rock slab geometry according to Uotinen et al. (2015)

Generated 3D mesh was found too dense for conventional modelling software to process, so a custom Python 2.7.5 script was created by Ari Hartikainen and Daniil Iakovlev from Aalto University's research group for Geoengineering. The script takes generated 3D mesh as an input, then finds a convex hull to create a solid. The convex hull is expanded to assigned frame to produce a collar for the mesh plane forming the variable angle between the collar frame and the convex hull points. Collar frame and convex hull create trapezoids which are triangulated by two triangles, with the exception of trapezoids containing corner point. The corners are triangulated by three triangles with corner point functioning as a divider. The collar frame is copied perpendicularly to create a bottom frame, which is positioned to assigned depth. The bottom plane is triangulated with a 2D-Delaunay network. The sides are created with triangulating two triangles for every trapezoid. The reversed surface model is created by inserting a negative depth value to reverse direction of the surface. The custom script produces a new STL ASCII format file as an output file containing the generated solid, which can be opened in a slicing software to create the tool head code for the 3D printing. Steps taken by the custom script are illustrated in Figure 14. The final solid has 5 mm margins and is 180 mm x 70 mm with 170 mm x 60 mm of active joint surface. The margin slopes were generated to reduce tensile failure near outer perimeter, detected in pilot phase of the development project. (Uotinen et al. 2015).

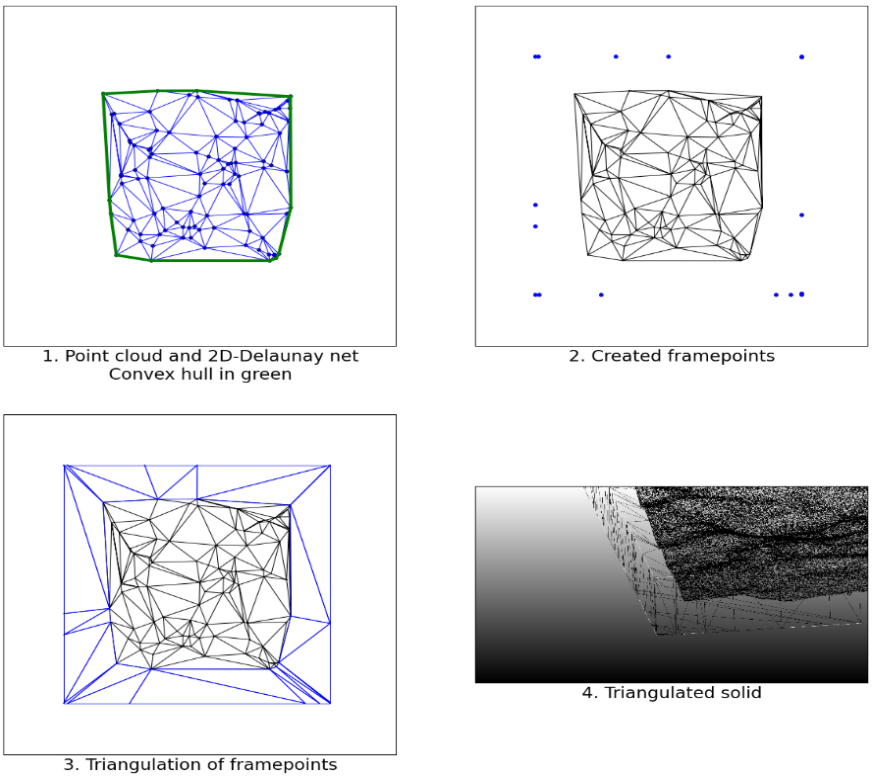

Figure 14. Steps performed by custom script according to Uotinen et al. (2015)

The produced pilot solids were printed with Ultimaker Orginal v3 2013 or Ultimaker^2 2014 fast prototyping fused filament fabrication 3D printers by applying Cura 14.07 slicing software, to create a negative surface of desired replication surface to be used as a casting mold for actual replica production. The applied printing settings are listed in appendix X. Then printed surfaces were inspected and anomalies removed. The final solids were printed with Stratasys Object30 Scholar printing equipment, with layer thickness capability down to 0.028 mm, with VeroBlack and VeroWhite materials. The solids were post-processed with pressurized water and air treatment. The produced surface molds were assembled to a complete casting molds by combining the printed surface with; aluminum base that had a hole in it enabling air bubbles to flow off the concrete, and two plexiglass plates forming sides for the complete casting mold. (Uotinen et al. 2015) The 3D printed casting mold is illustrated in Figure 15.

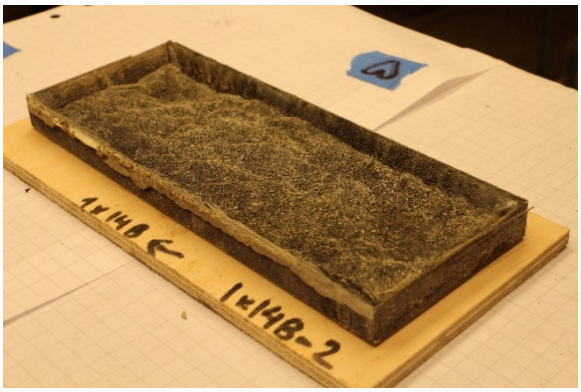

Figure 15. 3D printed casting mold.

The plastic replica surfaces of the mold were oiled with form oil prior to casting to reduce adhesion to the concrete. The casting was conducted with JB 1000/3 grouting mortar C60/75-4 with maximum grain size of 4 mm. Water was added to the dry mix in small doses during the first three minutes of the total four minute mixing time. For each 25 kg ready-mix bag, 3.1 liters of water was added, which results in water to cement ratio of 0.34. After mixing, 20 minutes were used for waiting to reduce swelling of the mortar. (Uotinen et al. 2015) Properties of the used mortar are listed in Table 1.

Table 1. Properties of JB 1000/3 ready-mix according to Uotinen et al. (2015)

Parameter	Value	Notes
strength class	C60/75-4	EN 206-1
compressive strength	45 MPa 1 d 70 MPa 7 d 90 MPa 28 d	+20 °C, EN 12190
binder	CEM II A 42.5 R	EN 206-1
water to cement	0.34	3.1 L water / 25 kg bag
aggregate size	0-4 mm	

Casting process was assisted with use of a vibration table; after filling the replica mold and a short vibration to spread the mortar, a longer 30 second vibration was applied to remove air bubbles out from the replication surface at the bottom of the mold, then 2 to 3 second vibrations were applied 8 to 10 times to spread the mass evenly over the mold, and at the end of the casting, another 30-second-vibration was applied to release air bubbles from the mass. After casting, the replicas were sealed tightly with plastic bag to prevent moisture from escaping from the vicinity of the concrete. The molds were taken down and the replicas moved into water immersion (18…22 C) for further curing. At

the age of 7 days, the replica samples were surface dried and tested in a portable shear box equipment with ISRM suggested method (Franklin, 1974) with minor modification; the matedness was checked using a powerful flashlight from the different edges around the sample. (Uotinen et al. 2015) The casting mold assembled on top of a vibration table before casting process is illustrated in Figure 16.

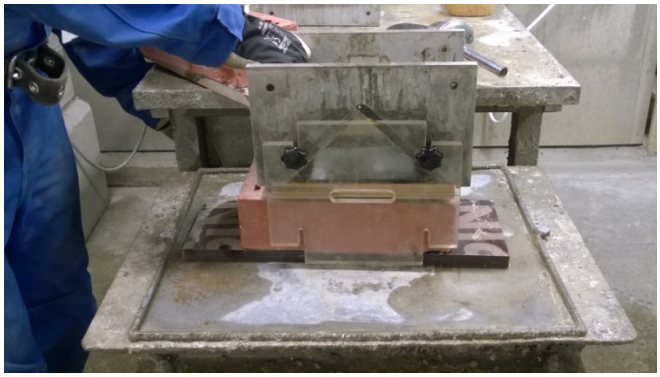

Figure 16. The complete casting mold assembled on top of a vibration table before casting according to Uotinen et al (2015)

Pilot replication and shearing procedure showed that chosen concrete mix was strong enough and no significant abrasion of the surface occurred during the shearing. Some loss of geometry was experienced and the need for attempt to compensate for it was seen evident. The final replication sample after shearing is illustrated in Figure 17. The replication method appeared to be feasible, but more testing needs to be conducted to draw conclusions based on effects of the replication process on shear strength. (Uotinen et al. 2015)

Figure 17. Replication sample after shearing, with red arrow indicating shearing direction

4.3 Developing photogrammetric replication of rock joint surfaces

Developed photogrammetric replication process was seen feasible, but a need for a further development was acknowledged. KARMO project has moved on to stage two, where accuracy for the developed process is to be defined, suitable, repeatable and self-compacting concrete recipe for the process is to be determined and applicability of results from tested concrete replicas for rock material is to be evaluated. (Aalto University, 2015) The second stage of the project has included applications of photogrammetry for sample replicas and 3D printed molds (Kallio, 2015), and a study for determination of the most suitable concrete recipe (Tolvanen, 2015).

Photogrammetric process applied for photography of replication samples and casting molds was adjusted from the original photography process: Used camera was Canon EOS 600D DSLR, used objective was Canon EF 35mm f/2 IS USM, used aperture for imaging was set to f/11 and exposure time to 1/125 seconds. Photographing arrangement was developed according to findings from original process; each sample was photographed from two heights with corresponding angles of photography of 30 and 60 degrees upward from horizontal plane, defined by replica surface, with 20 evenly spaced photographs in each layer, and illuminance varying between 4520 and 5100 lux. 3D modelling was performed in the same way as in the original process, presented in chapter 4.2. (Kallio, 2015) Applied photographic configuration is illustrated in Figure 18.

Figure 18. Photographing configuration for replica samples.

In addition to photography of casting molds and replica samples, the original rock slab was photographed with the same configuration, establishing a reference model between photographic process of original rock slab, casting mold and replica samples.

Along with additional photographic implementation, preliminary study on quality of replicated surface was conducted. The study inspected discontinuity roughness on original rock slab surface and on replicated concrete surfaces. The study was carried out with Joint Roughness Coefficient (JRC) measurements and with assessment of join surface amplitudes. Roughness measurements indicate that replication process has not been able to preserve original surface roughness very well. (Kallio, 2015)

JRC and amplitude measurements are rather subjective measuring methods and some variability on measurements is expected to be resulted from individual measurement practice. Kallio (2015) argues that inaccuracy of photogrammetric model can be responsible for differences in surface geometries, and that quality of replicas can be enhanced with development of photogrammetric process. It can be argued as well, that 2D measurements can lead to biased estimates about the roughness as it is in essence a 3D property.

5 Results

5.1 2D roughness evaluation

Hand measured JRC parameters (appendix 3) from replica samples are compared to the respective JRCs derived from digital models. Comparison between measured (x axis) and statistically derived JRCs (y axis) for different sampling methods (chapter 3.2.3) for surface length method (chapter 3.2.1) on central lines 2 and 5 (Figure 7) is represented in Figure 19. Central lines of the samples were selected to this inspection as the lines are independent of rotation of the digital model.

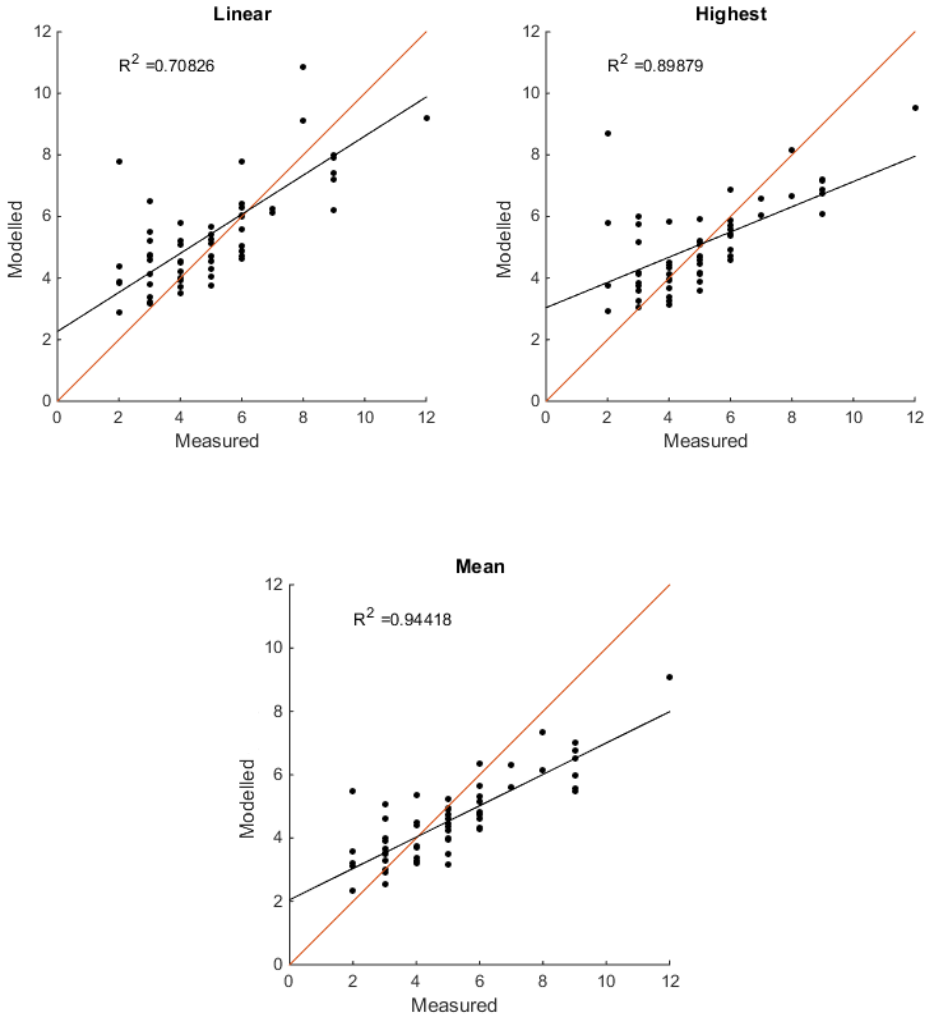

Figure 19. JRC comparison for surface length method (Maretz et al. 1990) for lines 2 and 5 (Figure 7) with hand measured JRC values on y-axis and digitally derived JRC values on the x-axis

The coefficient of determinations, denoted R^2, for the methods [Linear, Highest, Mean] are respectively [0.708, 0.899, 0.944]. R squared indicates the goodness of fit for first order best fit function for the variable ($Rp - 1$). In the other hand, the deviation of the best fit line to the match line indicates the deviation of the used function (10) from the best fit function. This reflects to a systematical error in the comparison. The applied function overestimates low JRC, from roughly 0 to 4, and underestimates high JRC values, from roughly 5 to 20. The used function maintains best behavior from the sampling horizons with Mean sampling. The values of R squared back up the best fit for sampling with Mean sampling.

Similar comparison for slope measurement (Tse and Cruden, 1979) is presented in Figure 20. The R squared values for this measurement technique follow same pattern, by giving the lowest value for Linear sampling and the highest values for Mean sampling, with R squared values for [Linear, Highest, Mean] respectively as [0.523, 0.619, 0.718]. This is consistent with visual inspection of model behavior of these plots as well, where Mean sampling seem to give the best match behavior. There is evident scatter in the results, but the trend of the plot seems to follow the diagonal fit line better than surface length method. This indicates smaller systematic error in the process, but involves rather low R squared value for the model.

Scatter in the results is well expected as the JRC measurements are conducted with measuring accuracy of one unit. This results in measurement accuracy of 1±1 unit accuracy for the measurement. Other effecting factor in the scatter analysis is the measurement noise. As commented by Tatone and Grasselli (2009), surface topography measurements obtained with any measurement device will contain some level of noise. The potential measurement noise is acknowledged here, but is not addressed further, as the analysis attempts to derive a method for capturing JRC from digital model that corresponds to hand measured JRC values on 0.5 mm sampling window. The widowing is considered to normalize the data and reduce the noise variation between different samples.

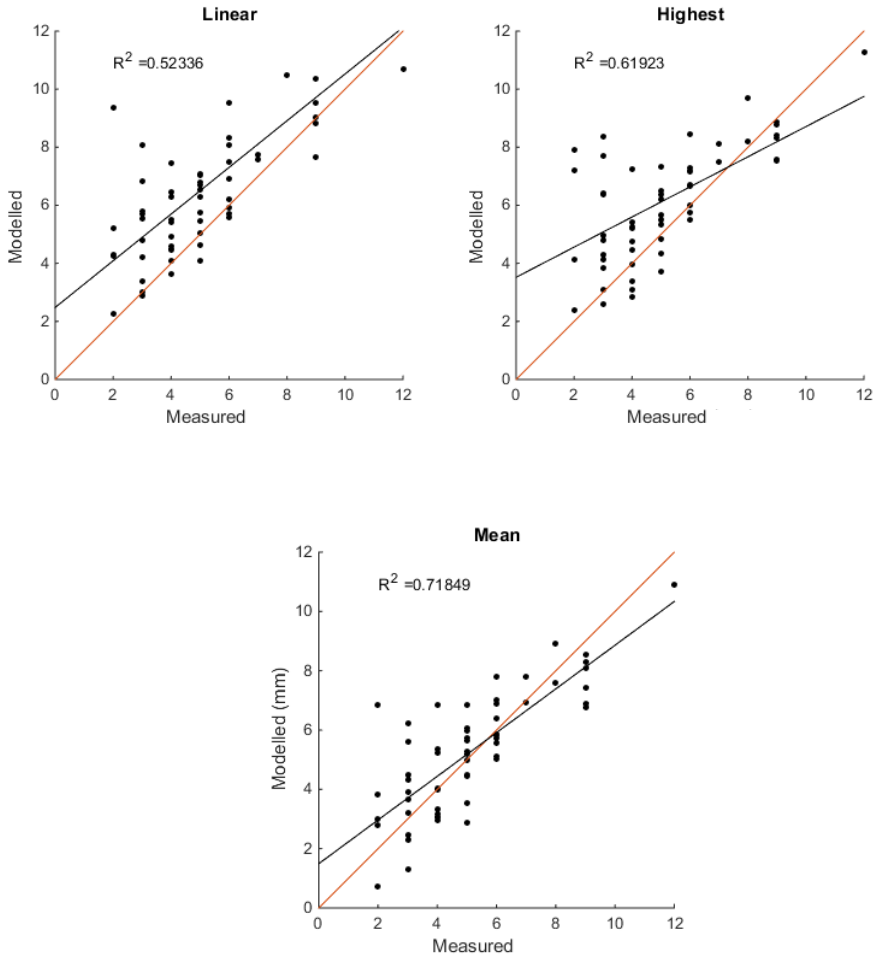

Figure 20. JRC comparison for slope measurement method (Maretz et al. 1990) for lines 2 and 5 with hand measured values on y axis and digitally derived values on the x axis

While the sampling with Mean method seems to give a reasonable match for the measurements, the function for determining JRC from the digital model deserves a revisit. For the two selected approaches; deriving JRC from surface length, and deriving JRC from the RMS of the surface points, the best fit functions are calculated.

Maertz et al. (1990) suggested surface length measurement to match with JRC through a constant c for the 2D roughness coefficient minus one $R_P - 1$. Revisiting this relationship by comparison of hand measured JRCs from replica samples to digitally derived $R_P - 1$ values trough first order least squares fit,

$$X^T X B = X^T y, \tag{17}$$

the best fit approximation results in,

$$JRC = -1.1917 + 563.7352 * (R_P - 1), \quad (18)$$

and by forcing B_0 term to be 0, the relationship takes a form,

$$JRC = 464.2201 * (R_P - 1), \quad (19)$$

As the original function is derived from numerous samples, it is safe to consider the original function as a good estimation of the corresponding JRC. Maertz et al. (1990) report the constant c to vary from 401 to 411, so the constant evaluated from the work flow is in the same region but remains fair amount apart from the original one. JRC derived from digital samples with function (19) against hand measured JRCs is shown in Figure 21. As this plot presents all the data, without applying a rotational correction for the samples, the scatter effect is estimated to be higher in the graph, additionally some systematical error due to rotation issues in the input data is possible.

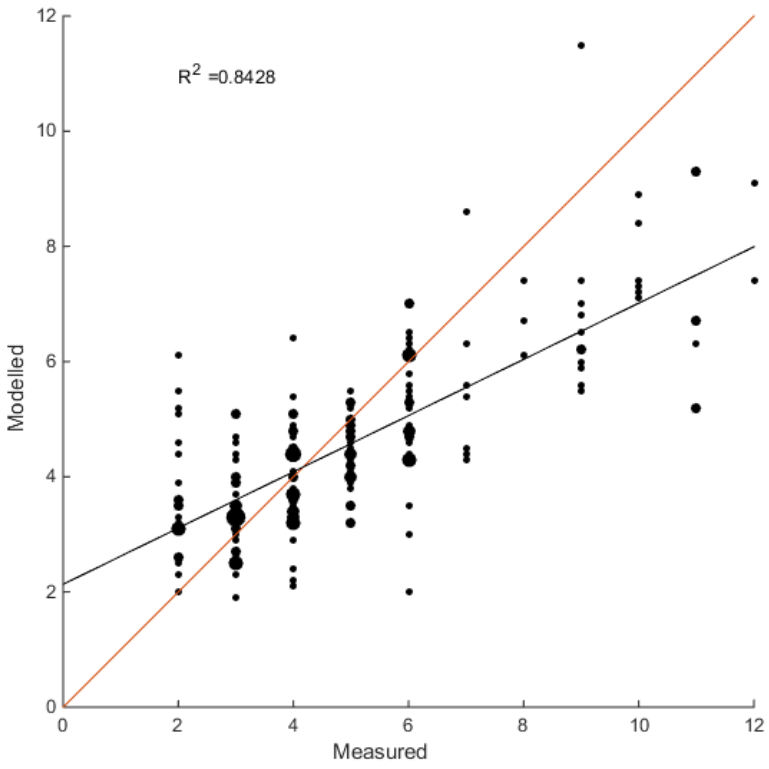

Figure 21. JRC according to best fit surface length method, presented for all JRC measurement lines, plotted against hand measured *JRC*.

Similarly the slope measurement (Tse & Cruden, 1979) is re-evaluated by finding the best fit function for $\log(Z)$. The linear regression analysis yields a best fit relationship for the measurements from lines 2 and 5 to be with function,

$$JRC = 28.1576 + 27.8045 * \log(Z), \quad (20)$$

where Z is the RMS value for the surface, introduced in chapter 3.2.

JRC derived from this best fit function for $\log(Z)$, plotted for hand measured JRC for lines 2 and 5 are illustrated in Figure 22. The function behaves very similarly to the original fit presented by Tse and Cruden (1979).

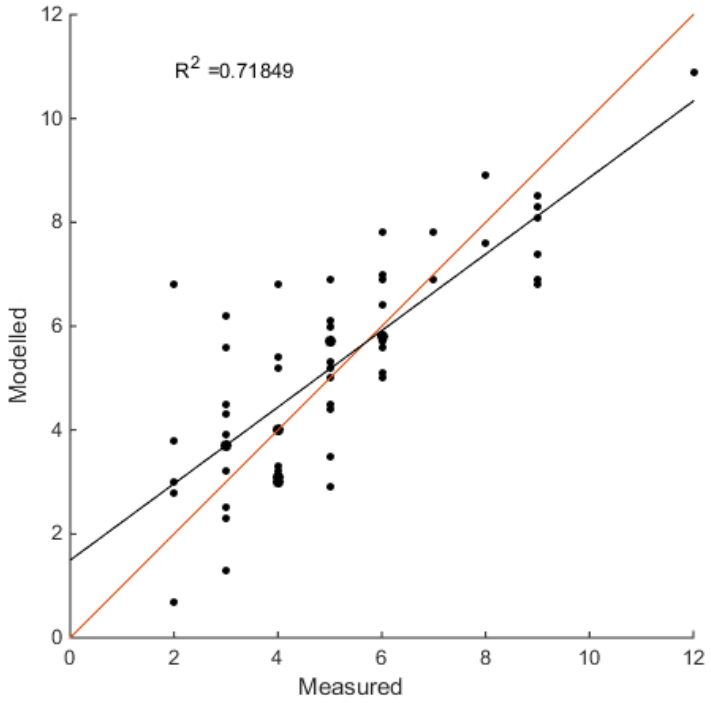

Figure 22. *JRC* according to best fit slope length method, presented for JRC measurement lines 2 and 5, against hand measured *JRC*.

Finally all data can be plotted for analysis methods accepted for further evaluations. JRC values from all replica samples plotted against digital reconstruction JRCs for slope measurement method is shown in Figure 23. By comparing Figure 21 and Figure 23, it can be seen that slope length method provides a better functional match with the inspected values, as indicated by the higher R squared, however slope measurement has a better match with trend line to the match line.

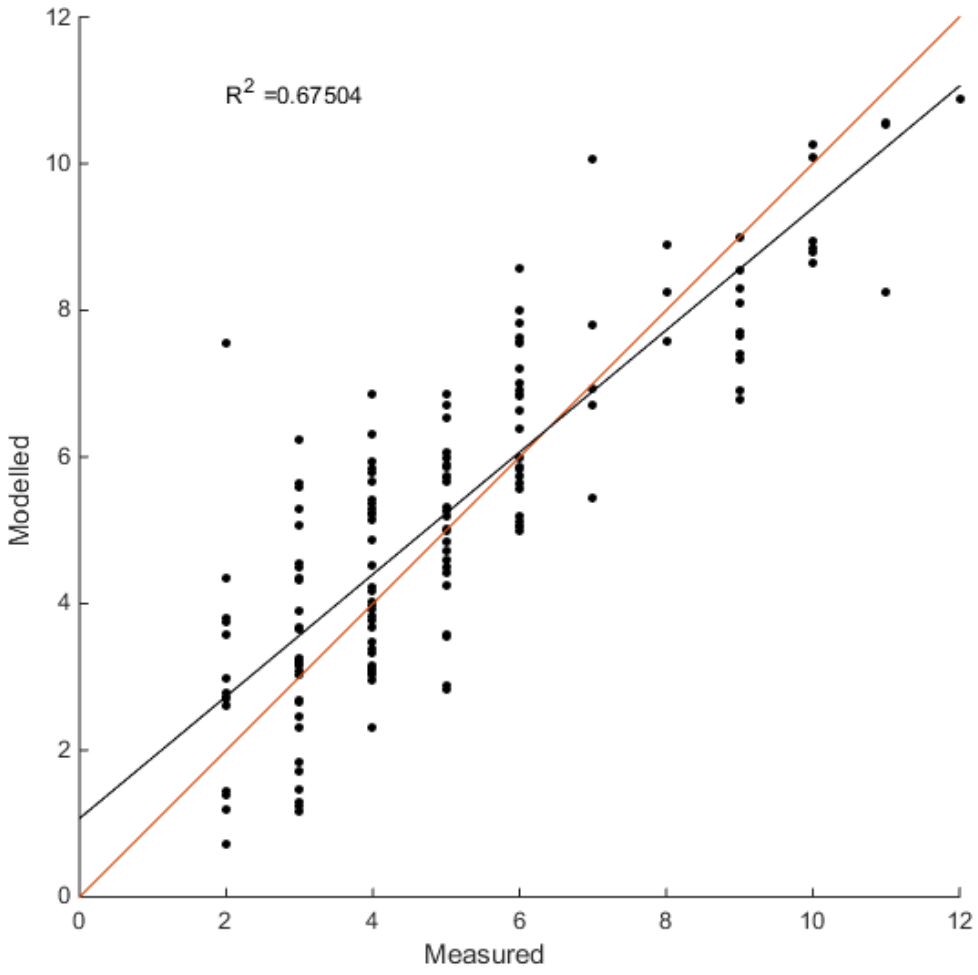

Figure 23. *JRC* according to best fit slope length method, presented for all JRC measurement lines, against hand measured *JRC*.

The potential issue of underestimating JRC for rough surfaces and overestimating JRC for smooth surfaces, as can be expected based on inspection of Figure 21 and Figure 23 is acknowledged and handled by adapting the fitting to match with the match line. As the trend line can be presented with line function,

$$y = a + b * x, \quad (21)$$

where a and b are constants describing the best fit relation, the correction to JRC measurements can be applied with,

$$JRC = (F(x) - a) * (1/b), \quad (22)$$

where F(x) represents the original function and a and b the constants from line function. The normalized surface length relationship for hand measured JRC for digitally derived JRC takes the form of,

$$JRC = 829.7053 * (Rp - 1) - 4.13655 \quad (23)$$

where Rp-1 is determined as presented in the chapter 3.2.1.

The normalized function applied for different best fit functions is illustrated in Figure 24. Function sweep is conducted for; original JRC relationship, first order best fit function with offset constant as zero, traditional first order best fit function, and second order best fit function, which are all normalized with trend correctional function (22). As the difference is very small, the original function with trend correction is applied for further analysis.

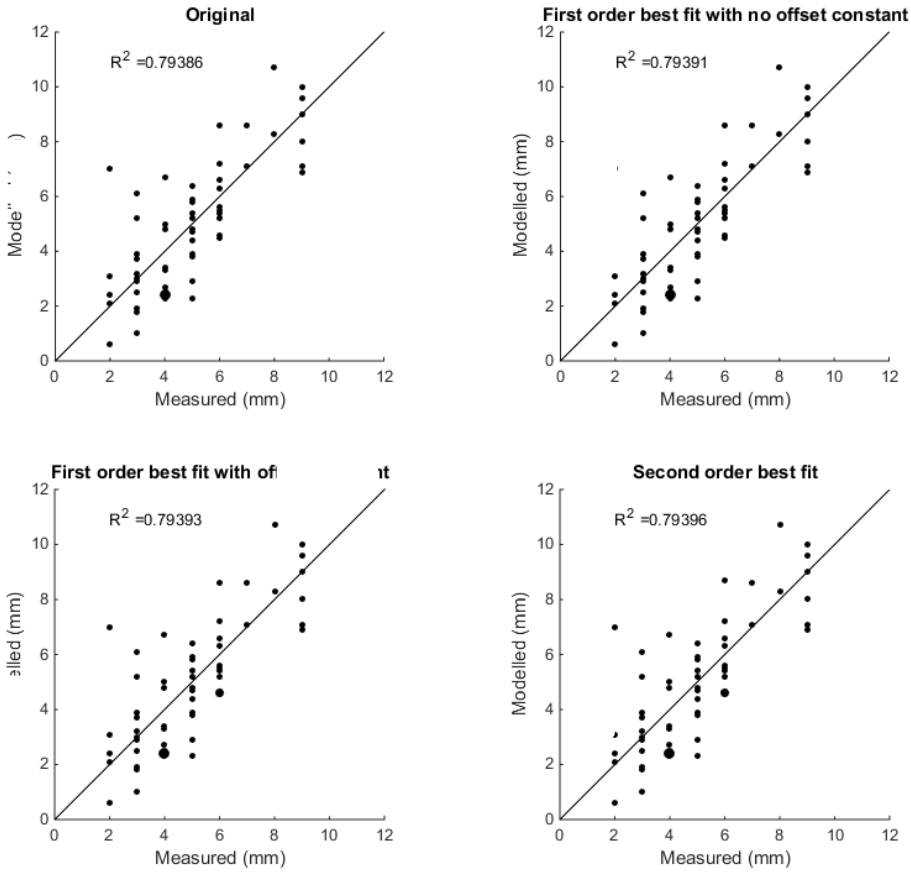

Figure 24. Normalized surface length function presented with different fitting options.

Similarly the slope measurement relationship is adjusted for inspected measurements, and the function in corrected with trend correction. The final relationship between

measured and modelled value is presented in Figure 25. The difference between values from corrected functions for original relationship and first order best fit function is very small, so the original function with trend correction is selected for further analysis.

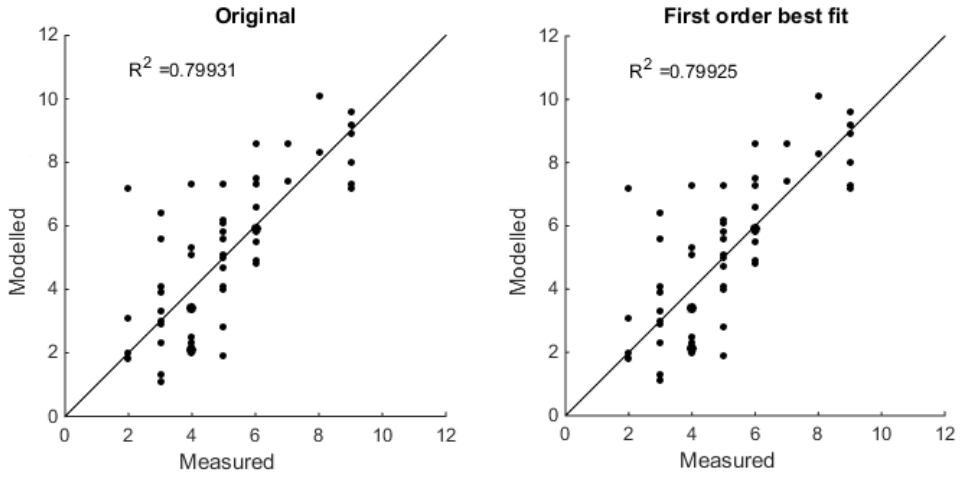

Figure 25. Normalized slope measurement function presented with different fitting options.

The overall R squared values inspected in these analysis are fairly low, and is expected to be a result of poor measurement accuracy with subjective JRC method and evident systematic error with digital model creation. As a result of these investigations, sampling with mean values for 0.5 mm sampling windows the slope measurement method according to Tse and Cruden (1979) with trend correction is concluded to offer a good base for analysis of surface roughness deformation in photogrammetric replication of rock joint surfaces while inspecting 2D section profiles. There would be a place here for deriving a function for JRC modelling from digital models basing on the samples measured in the KARMO research project, but as the total number of the samples are fairly low, and verification on the JRC measurements is fairly tricky to conduct in a reliable way, consequently it is seen that the existing statistical models for JRC evaluation, with best fit adaption, will be sufficient for the purpose of this thesis.

Analyzing 2D roughness between replicas and casting molds

Initial data includes digital models of the casting molds applied for final replica casting, which can be compared to the digital models of replicas to determine potential changes in surface geometry in the casting process.

The mold models are analyzed with the same workflow as applied for the replicas. The mold model data is prapared according to the procedure presented in chapter 3.2.1, and analysed in the same way as the replica surfaces, as presented in previously in this chapter.

Surface roughness is evaluated with JRC derived from corrected slope measurement (24), and compared with corrensponding replica JRC. This comparison is presented in Figure 26, with surfaces categhorized according to the size of the original rock surface to model surface size.

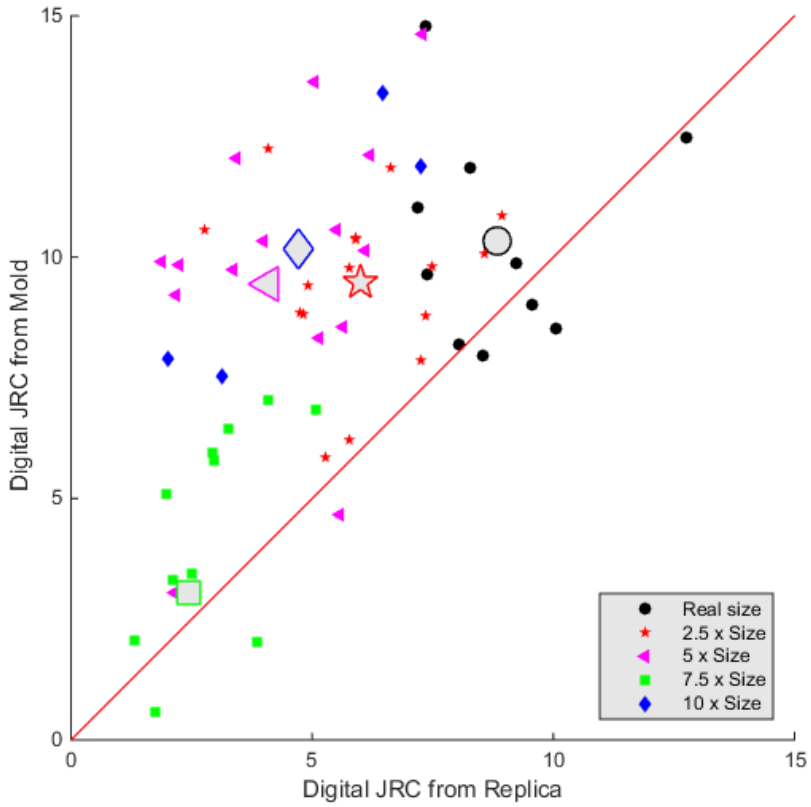

Figure 26. Mold JRC vs. Replica JRC for corrected slope measurement.

The figure clearly shows that mold roughness analyzed with the derived JRC relationship, yields higher results for each category of represented surface size. This would suggest a significant surface geometry loss between casting molds and replica samples.

As comparison the same analyze is conducted for the corrected surface length method (23). The comparison is illustrated in Figure 27. The comparison backs up the results from the corrected slope measurement relationship.

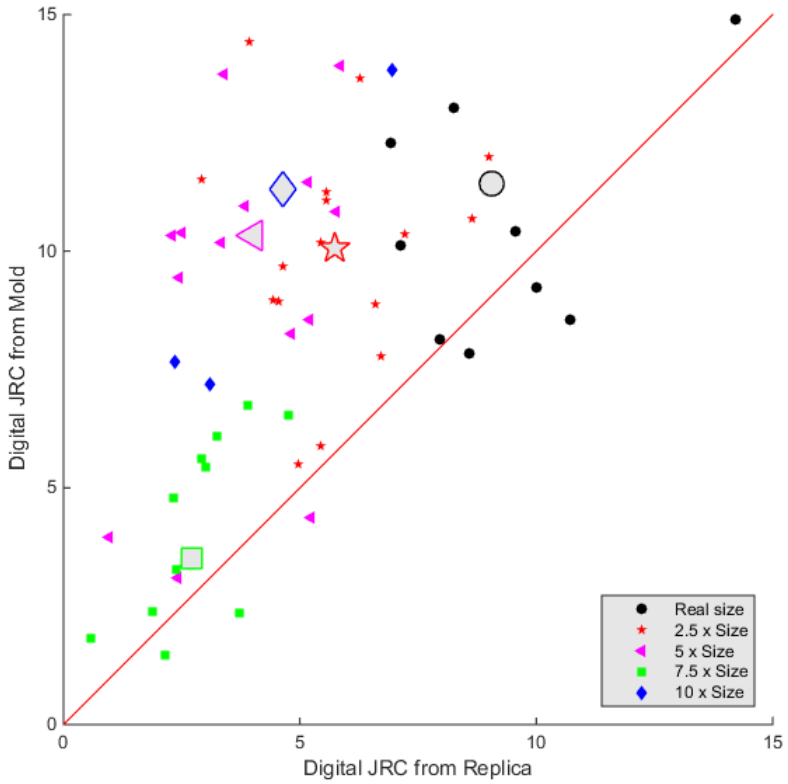

Figure 27. Mold JRC vs. Replica JRC for corrected surface length method.

The roughness comparison for casting molds and final replica samples shows clearly a geometry loss in the sample casting process. Additionally the scatter in the results is evident, and is expected to be a result of poor measuring accuracy for the original hand measurements and the systematical error that can be seen by comparing the traditional statistical methods and the results of these methods as applied for the digital photogrammetric models.

Analyzing 2D roughness casting molds and original rock slab

The comparison is then extended to take a look at the roughness development between original rock slab and the printed casting molds. The analysis is conducted in the same way as for the mold and the replicas, and is presented by the previous paragraphs.

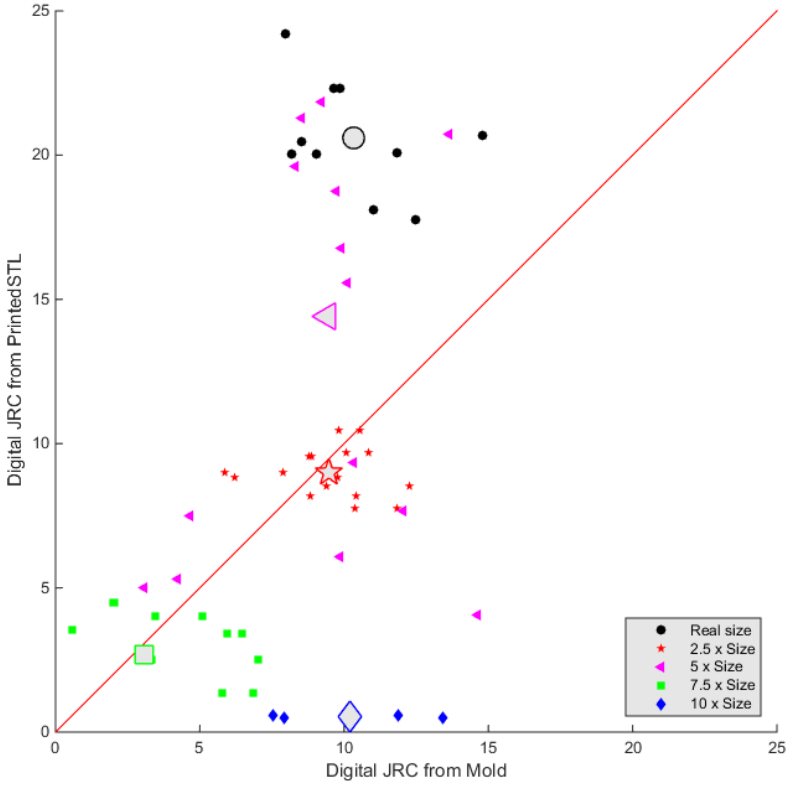

Figure 28. Digital model of casting mold vs printed STL surface model for corrected slope measurement.

Finally the surface roughness is evaluated for the original rock surface, with the same methodology as applied for replicas and molds. The rock slab surface data is prepared and sectioned as presented in chapter 3.2.1 and analyzed with corrected slope measurement function (24). The results are presented in the Figure 28. The comparison shows a strange behavior with the scaling size. The 2.5x and 7.5x representative surfaces seem to correspond well with the measurements, but from real size to 5x and 10x representative surfaces, there is a completely different trend in behavior. For these three categories, the modelling seems to lose more geometry as the representative surface gets bigger. Initial thoughts suggest that the systematical error inspected in the

QQ-plots might induce the increased over estimation for real size geometry and increased under estimation for 10x representative geometrical surface.

The strange behavior with the different representative surfaces is inspected by comparing these results to hand measured JRC values through the whole process. The measured JRC values are presented in appendix 6.

Measured JRCs for a measuring section 2 (figure x) are presented in Figure 29. The figure clearly shows the present scale effect on roughness measurement with JRC methodology. As the casting mold and the replica sample represent the same geometrical surface, without scaling, the roughness variation in replica production can be evaluated for all samples. Evaluation of mold production on the other hand should be limited to the non-scaled samples. Further investigations can be carried out by taking the scale effect into account, but this is considered to be outside of the scope for this thesis.

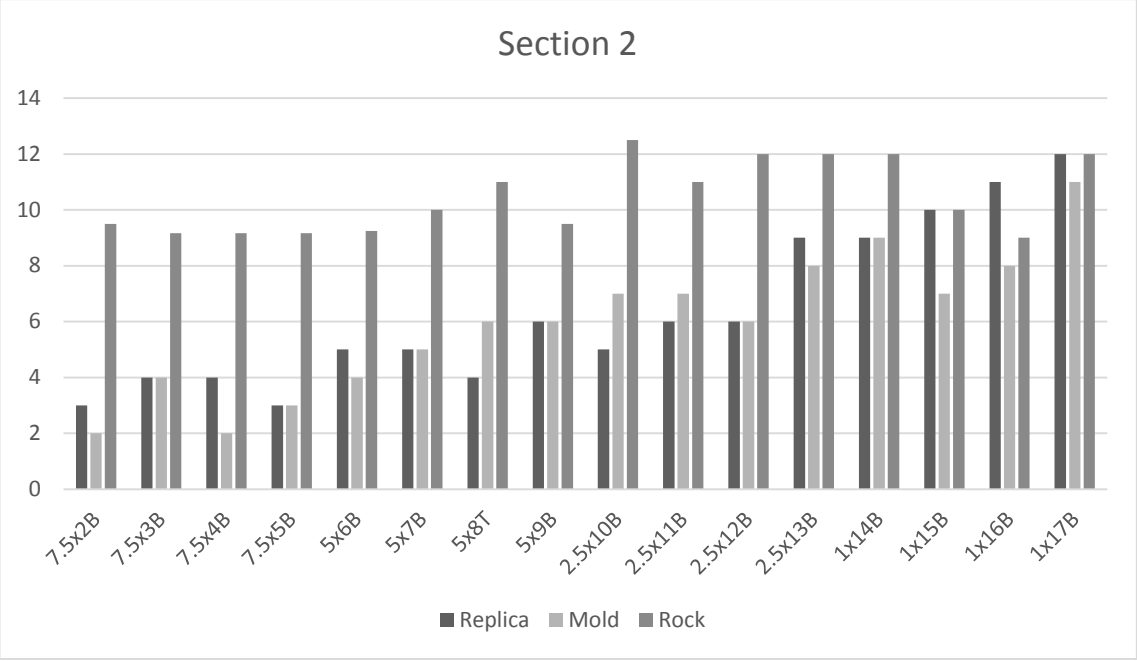

Figure 29. Hand measured JRC for a measuring section 2, presented for the final replica, casting mold and the original rock slab.

When considering the replica production, the trend seems to be for the replica to be rougher than the casting mold, with some samples maintaining the roughness very well and some introducing inverse behavior by decreasing the roughness. Some samples

seem to maintain the wanted behavior, but there is evident scatter in the process as well. For the printing process, all four samples loose geometry in the printing process.

While the hand measured JRC measurements are very subjective, and cover only a fraction of the surface area, the scale effect on the roughness evaluation trough this methodology is evident. For the non-scaled samples, it gives an easy and fast way to analyze the surfaces for preliminary analyses. Finally it should be pointed out that the photogrammetric modelling of replica samples was conducted post-shearing, and it is not expected for the roughness of a replica sample to completely match the roughness of a casting mold, or the original rock slab.

As the two dimensional roughness analyses are unable to utilize the full surface in the roughness evaluation on attempt of roughness characterization with various three dimensional evaluation techniques is presented in the following chapter.

5.2 3D Roughness evaluation

5.2.1 Surface area analysis

Preliminary analysis

Preliminary analysis of 3D roughness was conducted with roughness coefficient R_S, which is the 3D analog of the roughness coefficient R_P presented in chapter 3.2.1. While R_P describe the true surface length of a 2D profile to the nominal surface length, the R_S describes the ratio between the true surface area and the nominal surface area,

$$Rs = \frac{A_t}{A_n}, \tag{25}$$

where A_t describes the true surface area and A_n describes the nominal surface area. (El-Soudani, 1978) Consequently a smooth surface would have roughness value of 1. Tatone and Grasselli (2012) present that a rougher surface would display values up to 2 for rock discontinuity.

The preliminary analysis was conducted for digital models from all three stages of the photogrammetric replication process; rock slab, casting mold and replica sample. Results from the preliminary roughness evaluation are presented in Figure 30.

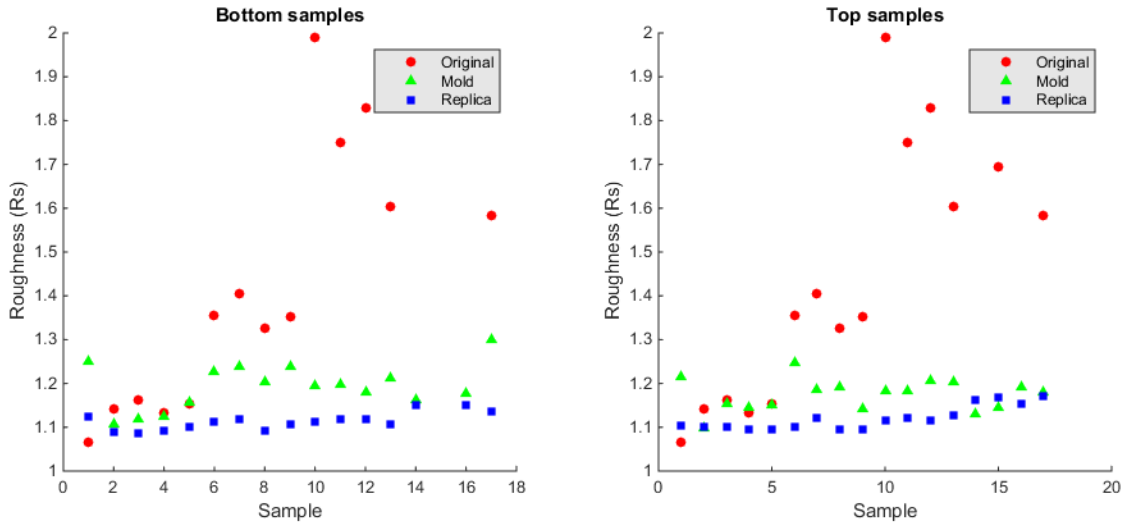

Figure 30. Preliminary results of 3D roughness evaluation for replica samples, replica molds and original surface.

Replica samples are named according to representable surface area from the original rock slab, as described in chapter 4.2; sample 1 representing a 10x geometry, samples from 2 to 5 representing a 7.5x geometry, samples from 6 to 9 representing a 5x geometry, samples 10 to 13 representing 2.5x geometry and samples from 14 to 17 representing a 1x geometry.

If the photogrammetric replication process would be perfect, the roughness of original, mold and replica samples would be equal for all samples. Clearly this is not the case. The preliminary study suggest a bigger change in the geometry between original geometry and the casting mold, as the representative geometry gets smaller. The relationship of geometry change between casting mold and replica sample in the other hand is not that clear. Replicas are less rough than casting molds, but the relationship seems to be more or less same for all samples. There is clear variation in the results, as can be seen from the varying difference between mold roughness and replica roughness.

One factor to be considered here is the fact that the replica samples were sheared prior to photogrammetry, which inflicted some damages to the sample surface as illustrated in Figure 31. It should also be noted that the damages to the surface are not currently mapped, and cannot thus be analyzed accurately. The geometrical change inflicted by the shearing is considered to be existing but unknown and varying with a manner which at this stage is unidentified.

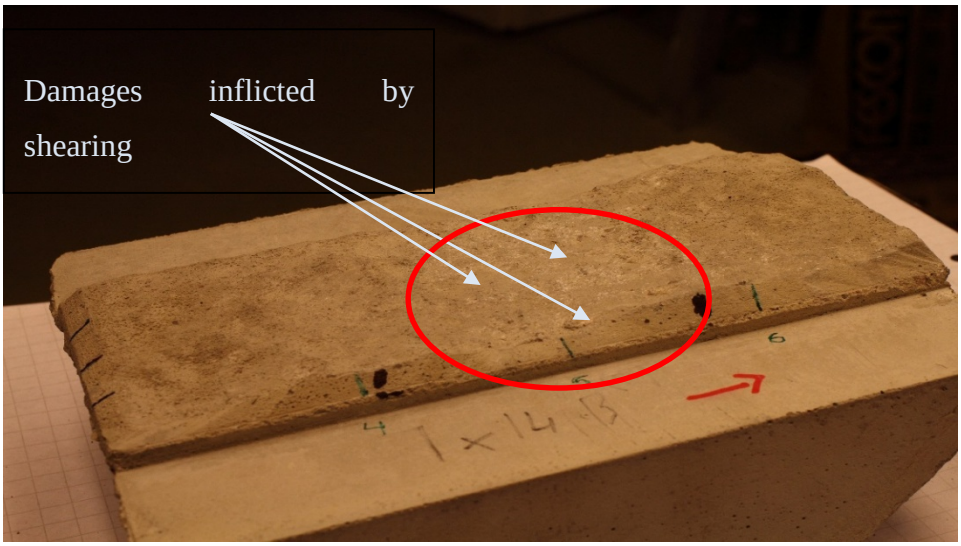

Figure 31. Illustration of shear damages in replica samples

As the samples are divided to top and bottom samples, with top sample representing an inverse of the bottom sample, the top and bottom samples should have the same roughness. The difference between these values gives an indication on the variability of the method applied for production of the surfaces. Especially, the roughness of printed casting molds can be analyzed for information on accuracy of the printing procedure.

The R_S coefficient plot for bottom and top samples for all samples is illustrated in Figure 32. The variation of the roughness is evident from the scatter plot. The difference between the R_S values varies from 0.0063 to 0.1176, with arithmetic mean at 0.0318. The values give indication on the effects of replication process on surface roughness but are not self-evident, as the applied photogrammetric modelling can affect the produced difference. What is clear, is that there is difference between the two surfaces models, how much of the difference originates from variation in photographic procedure is unclear, and would require additional modelling to be defined accurately.

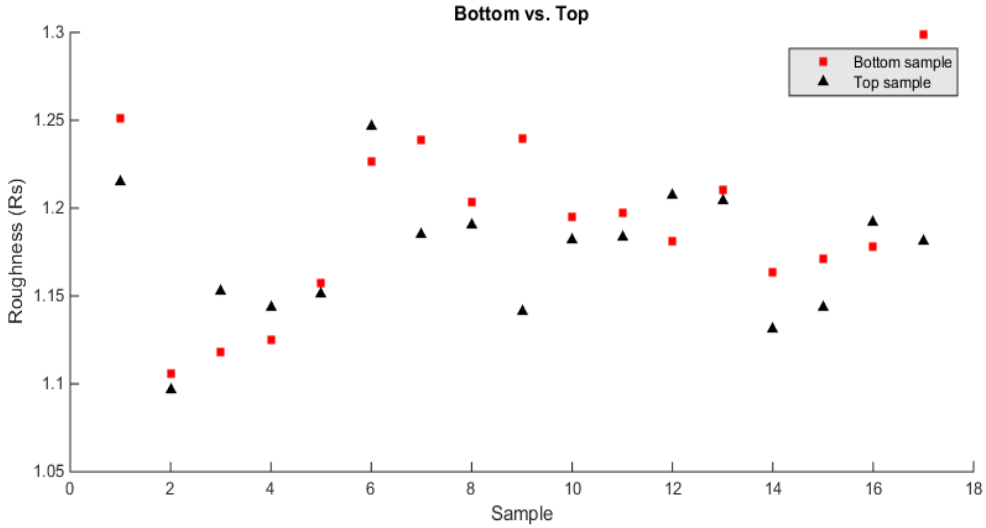

Figure 32. Rs coefficient comparison for bottom and top samples

Further analysis of the roughness coefficient R_S shows that roughness changes from casting mold to replica sample with R_S roughness difference varying from 0.0041 to 0.1626 with arithmetic mean at 0.0695. Similarly, the difference with R_S roughness metric normalized with mold roughness varies from 0.0037 to 0.1252 with arithmetic mean at 0.0577. More detailed description of the roughness difference is illustrated in Table 2, where the roughness difference is presented for all geometrical categories.

Table 2. Rs roughness spread between representative geometric surface area

Geometry	Samples	mean d(Rs)	mean (d(Rs) / Rs(mold))
10x	1	0.1181	9.57 %
7.5x	4	0.0373	3.27 %
5x	4	0.1033	8.48 %
2.5x	4	0.0782	6.53 %
1x	4	0.0437	3.54 %

The mean difference between Top and Bottom samples varies from 3.5 percent up to 9.6 percent, which suggests a significant measure of difference produced in the printing and photographic modelling process. The burning question here is, how much of this difference can be explained with photogrammetry and printing process. Higher point density increases the roughness recorded by the R_S metrics, as registered by Tatone and Grasselli (2012). Their findings inspected R_S roughness as a function of point spacing, and it was stated that there is a clear decrees in roughness as the nominal point spacing increases.

Analysis with normalized search window

Further inspections were carried out by acknowledging this effect for R_S parameter, and normalizing the recorded STL surfaces with 1 mm^2 search windows for the casting mold and replica surfaces, and corresponding 1 to 100 mm^2 search windows for the printed surface geometries. The normalization was conducted by calculating the mean point for all search windows and forming a new STL surface according to resulting points. The inspection results area presented in Figure 33. Comparing Figure 30 and Figure 33, it is evident that the normalization has a major effect on surface roughness for all categories. The roughness is decreased for all categories as expected, and the big differences between categories normalizes significantly. More surprisingly the differences between the categories is clouded by the scatter of the results. General view from the plots is that casting molds have higher roughness than the original surfaces and the final replicas have lower roughness than the casting molds.

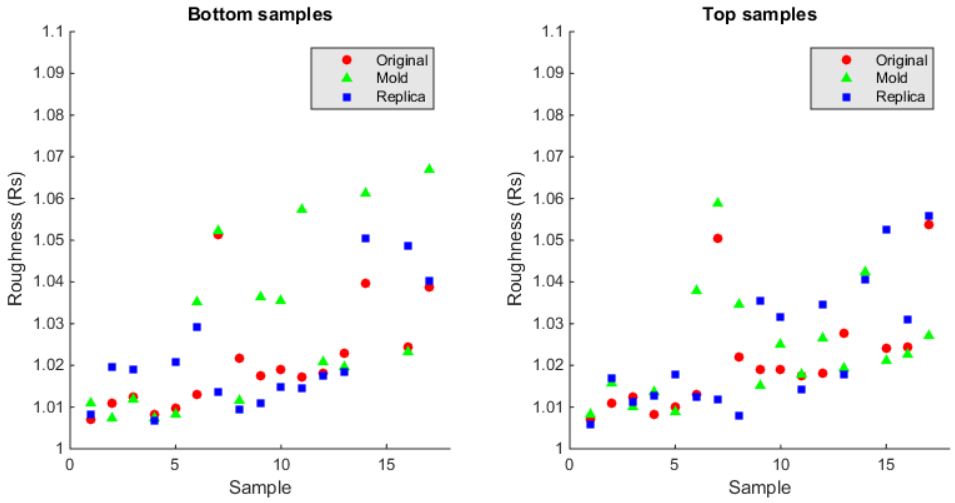

Figure 33. Normalized roughness (Rs) for original rock surface, replica mold and final replica.

To have a better understanding of the results, more detailed inspection of the different categories for representative geometrical surfaces is inspected. The inspections for different categories by representative geometrical surface is compiled by evaluating top and bottom samples together, for each scaling group with sufficient quantity of data available for analysis (7.5x, 5.0x, 2.5x, 1.0x). The results are presented in Figure 34**.**

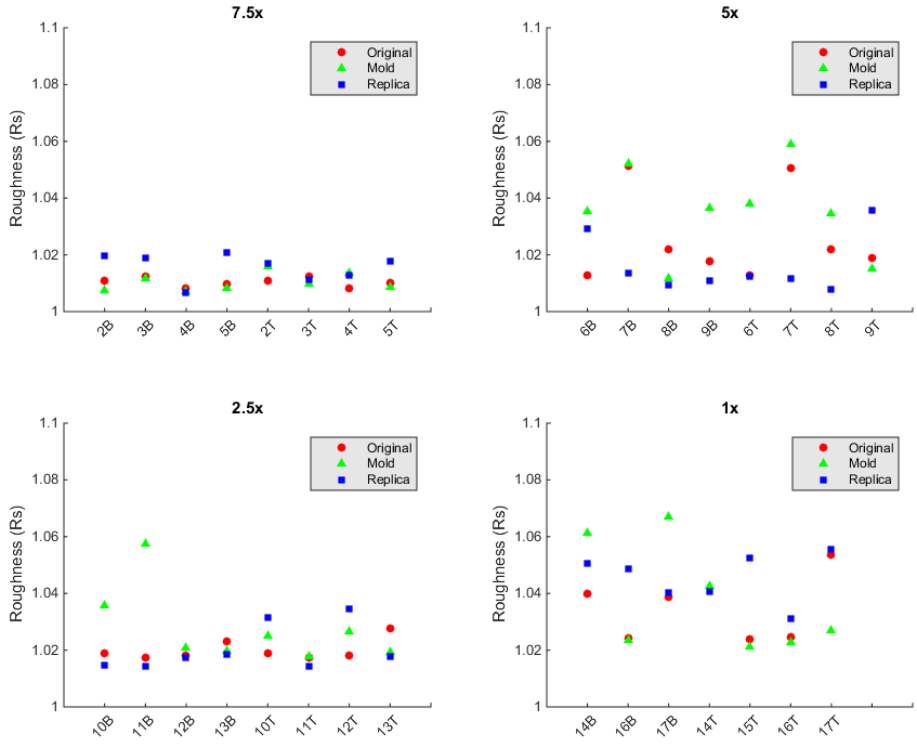

Figure 34. Normalized roughness (Rs) presented for each representative surface geometry category

The representative surface geometry of 7.5x seems to offer a good match for original surface and printed casting mold, especially for samples 2B, 3B, 4B, 5B, 3T and 5T. In the other hand the surface roughness of replica samples seems to escape other two surfaces by introducing increased surface roughness, the only good matches with casting mold and final replica sample seem to be with the samples 4B, 2T, 3T and 4T. Consequently only samples 4B and 3T seems to be able to preserve the surface roughness through the whole photogrammetric replication process. It should be noted here though that the final replica samples were sheared prior to the photographic modelling, and thus this results can not offer the full information regarding the changes in the surface geometry in the photographic replication process.

Expansion of the inspection from 7.5x geometry to include the other analyzed geometries is presented in Table 3 and Table 4.

Table 3. Surface roughness match between the samples.

	Good match
Original vs. Mold	2B 3B 4B 5B 3T 5T 7B 9T 12B 13B 11T 16B 15T 16T
Mold vs. Replica	4B 2T 3T 4T 8B 12B 13B 11T 13T
Whole process	4B 3T 12B 13B 11T

It seems that current state of the photogrammetric replication of rock joint surfaces is able to replicate the surface roughness, as can be observed from the 5 samples that were able to preserve the surface roughness in the process. But, there are plenty of room for improvement in the reliability of the process, as only 5 samples out of 33 analyzed samples seem to give a good match through the whole process. In addition to this lack of reliability, the performed analysis are subject to number of potential human errors in the replication process. The surface matches between different categories is further elaborated in the

Table 4. The table shows results from surface difference analysis conducted by R_S metrics.

Table 4. Good 3D surface roughness matches between the process steps in numbers of samples with good match according to evaluation of Rs metrics.

	Original vs. Mold	Mold vs. Replica	Whole process
7.5x	5	4	2
5x	2	1	0
2.5x	3	4	3
1x	4	1	1

An additional attempt for pin pointing the location of the relevant errors in the process was carried out by inspecting the variation in mold geometries for bottom and top samples with normalized roughness (Rs). The results are presented in Figure 35.

As the top and bottom molds are printed from the same geometry the variability in the results should present the variability in the printing process. As can be seen, by comparing Figure 32 and Figure 35, the applied normalization does reduce some scatter from the results. There are some samples that match well, but the ratio of success in the process seems to be only around one forth from the samples.

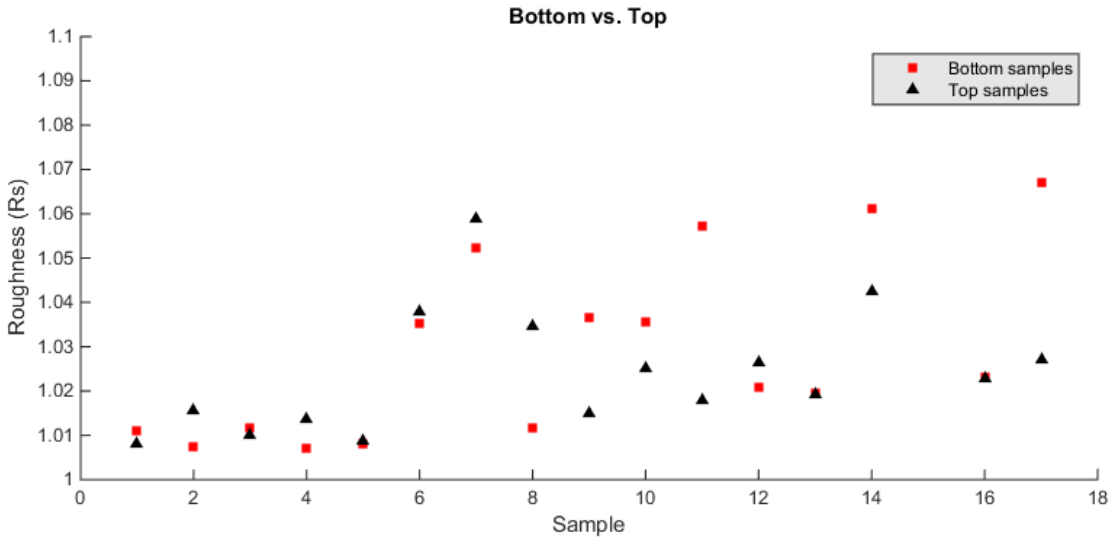

Figure 35. Scatter between top and bottom sample molds for roughness (Rs).

The good matching samples are 1, 3, 5, 6, 7, 12, 13 and 16, while the bad matches seems are with samples 2, 4, 8, 9, 11 and 17. The relation between used printer and printing material was crudely inspected, but there seems to be no evident existing relationships there. Overall the scatter in the results seems to be resulting from the variability in the printing process. Table describing the data behind the Figure 35 is presented in appendix 6.

Finally the change of geometry through the whole process can be illustrated with an example surface for good and not so good geometry preservation. The Figure 44 in appendix 8 presents a good example of roughness preservation trough the photogrammetric replication process. The Figure 43 in appendix 8 in the other hand presents an example of surface that experiences significant geometrical changes in the process. Finally a comparison of geometrical changes in the surfaces is presented as a comparison for good and not so good replication in Figure 36. The figure is plotted for the difference between the original surface geometry and the final replica surface geometry, according to the roughness analysis presented previously in this chapter, with coloring according to the difference between these two surface geometries. It can not be stressed enough here, that the final replica is modelled post-shearing and the surfaces are not supposed to be exactly the same. For sample 11T, the shearing damage seems to be inflicted in more confined area, as for sample 7T, the damage is more spread over the whole surface.

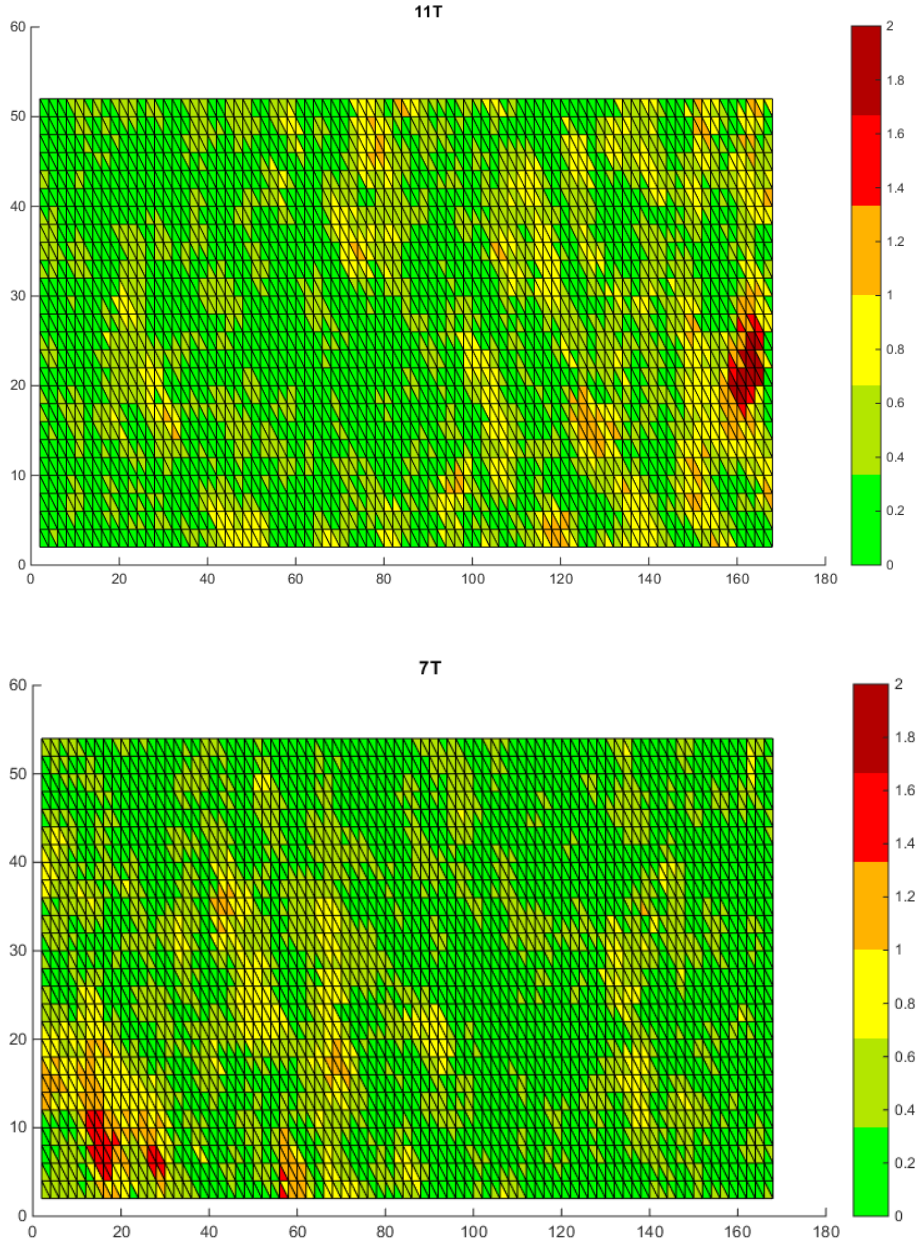

Figure 36.Comparison of heights for original surface and replica sample for samples 11T (upper) and 7T (lower), coloring according to geometrical difference between original surface and replica sample. Sample 11T representing a well preserved geometry in terms of roughness, and 7T representing not so good preservation of roughness

5.2.2 Directional 3D roughness analysis

Finally the digital surface models are inspected with directional 3D roughness, the trend behavior seems to be for the samples to lose geometry in all steps of the project. But for some samples there are irregularities for this trend, especially with casting mold offering a higher roughness than the original surface, yet mostly the final replica is still less rough than the mold, and the original. There are samples that were able to preserve the geometry in 3d printing, and samples that were able to preserve geometry on casting, and even some samples that were able to preserve geometry throughout the whole process. This is encouraging when evaluating the potential of the process. But it also shows that the process is far from perfection, and there is much to do in terms of quality management and human error elimination in the process.

Examples of the results are presented in Figure 37 and Figure 38. The Figure 37 shows a common trend behavior as inspected from the analyzed results, and Figure 38 shows a typical mismatch behavior in the data.

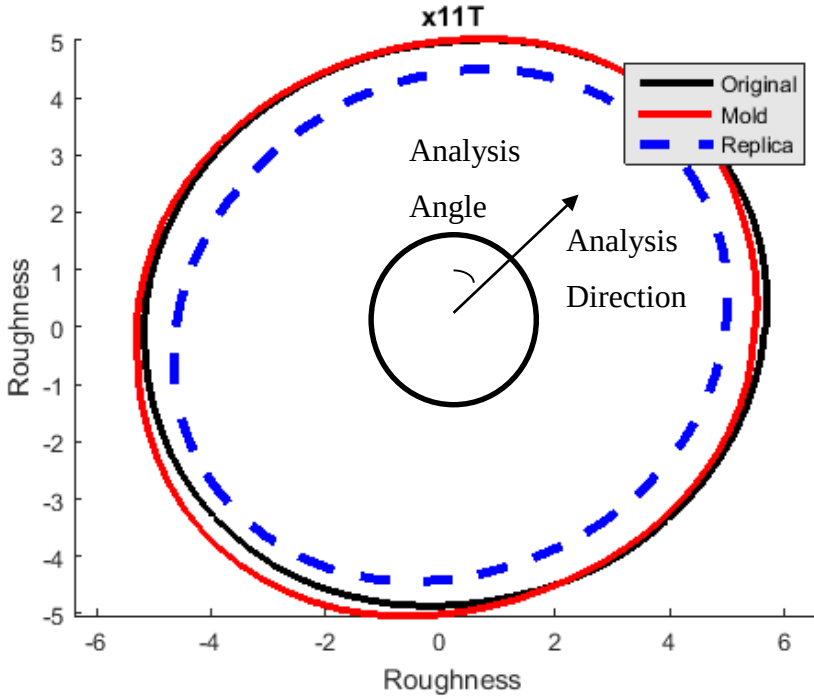

Figure 37. Directional 3D roughness of a typical trend behavior presented in a polar plot, for the original rock surface, surface of the casting mold and surface of the final replica sample.

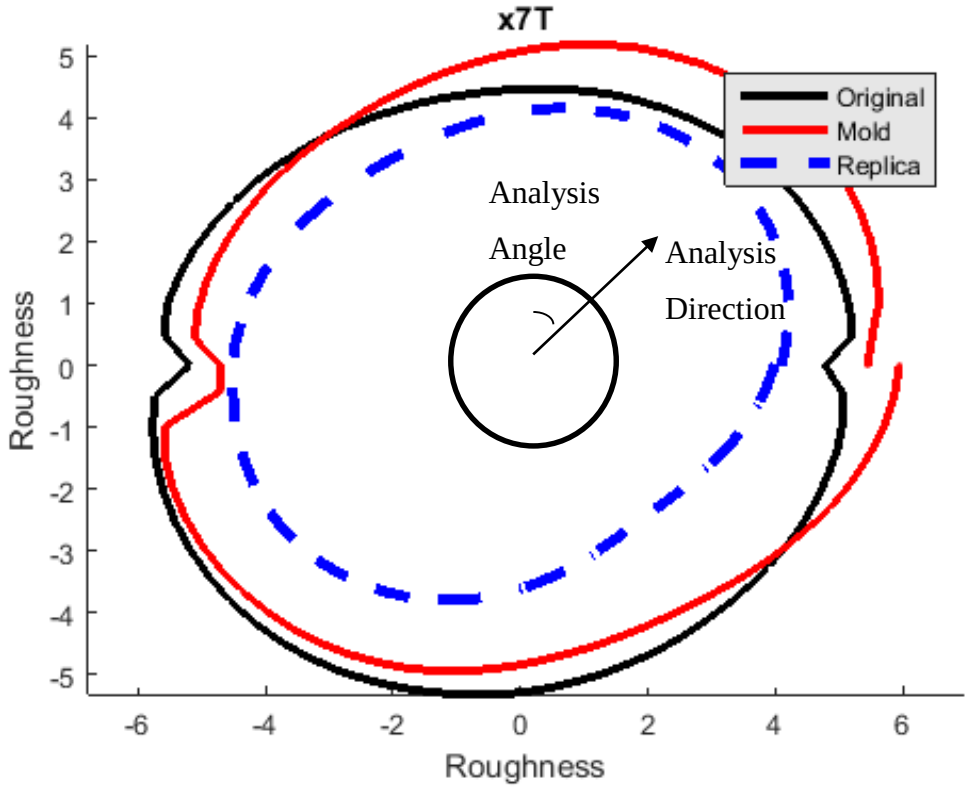

Figure 38. Directional 3D roughness of a mismatch behavior presented in a polar plot for the original rock surface, surface of the casting mold and surface of the final replica sample.

The example plots illustrate well the effecting scatter in the produced digital surfaces. A more elaborate plot for all representative surface geometrical scales is presented in the appendix 8. The appendix shows the directional 3D roughness plots for all samples representing the top samples from the created replica samples. Overall the directional 3D roughness estimation seems to provide a good way for measuring change in surface geometry in the photogrammetric replication of rock joint surfaces.

5.3 Determining model quality through image quantity

Accuracy of photogrammetric modelling was inspected by analyzing the effects of changes in quantity of initial photographic images to the point density of the digital model. The original rock slab was re-photographed with 1035 photographs by handheld photography from three layers corresponding to 30, 40 and 45 degrees from horizontal surface plane. There was some variation in the angles and in the shooting distance, as the applied photogrammetric method was constrained by limiting space around the sample. The imaging for a layer was conducted in two steps, with both steps covering evenly all rotational directions of the slab. The spatial photography locations result from hand held configuration, and it is considered very unlikely for an image to match another image from the set. The imaging configuration is illustrated in Figure 39.

Figure 39. Camera locations in re-photography for point density saturation study

The images were shot with Canon EOS 600D DSLR camera and a Canon EF 35mm f/2 IS USM objective. The applied F-stop was f/11 and exposure time 1/125 sec with ISO value as 2000. The photography was conducted in an environment with constant illuminance of 1590 lx. As an optimal ISO value would be 100, it is advised to decrease exposure time and increase lighting to enable a low ISO sensitivity in the photography. Use of stable shooting platform is also strongly suggested. The photogrammetric modelling was performed according to the modelling procedure presented in chapter

4.2. The resulting graph for image quantity versus point density is presented in Figure 40.

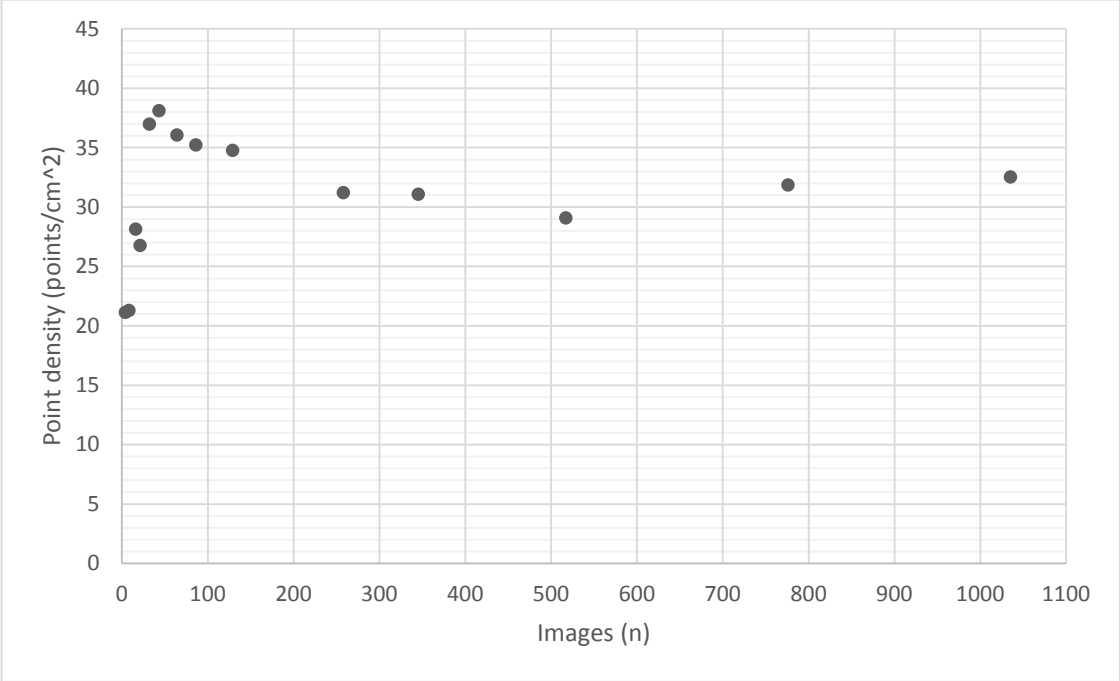

Figure 40. Point density as a function of image quantity for re-photography for point density saturation study.

Expectation for the study was to steadily approach a saturation limit for the point density, and after reaching the limit the increase of images would not affect the point density. The expected saturation point is reached in the study with about 300 photographs. Surprisingly thought, there is an additional peak in the point density between 30 and 60 photos. The peak seems to be resulting from measurement noise, which is smoothed down by over sampling as the quantity of images increases. The study would suggest the optimal imaging quantity to be around 300 images for the photographic replication of rock joint surfaces at high ISO sensitivity.

The effects of lens distortion and ISO sensitivity were inspected with additional modelling study. In the study, the rock slab was photographed with imaging configuration corresponding to the configuration applied to casting molds and replica samples. The slab was shot with 40 images in to different environment, with same F-stop and exposure time (f/11 and 1/125 s), by adjusting ISO sensitivity to the lighting environment. The first photoshoot was conducted with ISO sensitivity of 400, and the

second with ISO sensitivity of 2000. The results for point density from inspected surface models are presented in Figure 41.

The comparison study was conducted with two sampling techniques: random sampling from the taken photographs, and sampling images evenly to maintain images from all sides. The modelling was also conducted for images with lens correction routine and images without the routine. Basing on the graphs random sampling and even sampling presented in the Figure 41: The random sampling results in variability with point density to image quantity relation, as expected, emerging from the potentially rotationally biased sampling, while the even sampling increases the point density in a steady manner in relation to image quantity. Furthermore, the higher ISO sensitivity seems to generate a higher point density. As an increase in ISO sensitivity increases the digital noise in the resulting image, the study would suggest that there are more errors in the photogrammetric modelling when performed with higher ISO sensitivity. This study does not show how this effect performs when the image quantity is increased, the Figure 39 shows a smoothing of the top point density, when the image quantity is increased. On base of these inspections, this type of behavior is expected, but the difference on final point density between low ISO sensitivity and high ISO sensitivity is still a mystery. However, the point density for low ISO sensitivity seems to reach a saturation point with 30 points per square cm, and this corresponds well with the reach saturation point on oversampling with high ISO sensitivity. The follow up study for evaluation of how ISO sensitivity affects point density on over sampled case, is planned for the KARMO project, but the investigation exceeds time resources dedicated to the thesis work. For the effects of lens correction, the effect is fairly low and it is hard to draw a reliable conclusion, but the overall trend seems to be a lower point density on low image quantities (<25) and an increase in point density in higher image quantities (>25). This would indicate less error points, and more accurate points with the lens correction.

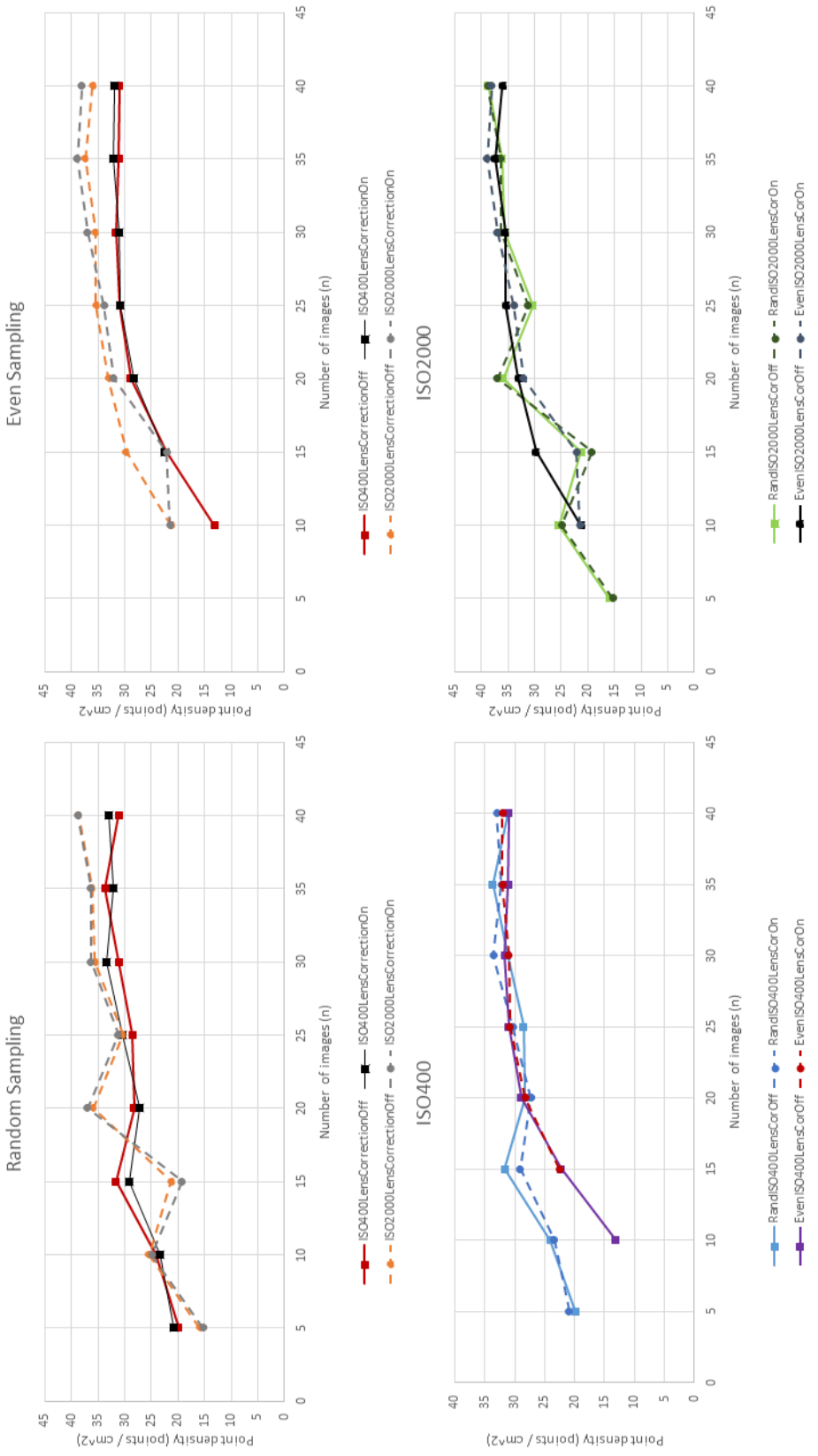

Figure 41. Comparison of relationship of point density and image quantity with chancing sampling and ISO sensitivity and lens correnction.

As the modelling conducted for the surfaces in analysis of casting mold and replica sample were carried out with 40 images, the corresponding point density was around the peak point density for the process. The suspected measurement noise affecting the modelling is also highest around this imaging quantity. This could affect the conducted analysis by introducing additional scatter in the modelling results, it should be noted though that the used ISO sensitivity was around 400 in the photographic process, and the effecting noise should be lower than with high ISO sensitivity. However it should be acknowledged, that the modelling of the casting mold and the replica sample were conducted with matching procedure, and the results should thus be comparable.

6 Discussion

The conducted roughness evaluation methods seem to be able to characterize the change in the surface roughness in the photogrammetric replication of rock joint surfaces, and is able to present results of the overall performance of the replication process. For example, for sample 4T, the loss in surface roughness between original surface and casting mold is about 2 percent, and the loss in roughness between casting mold and replica sample is about 6 percent as inspected from the directional 3D roughness analysis results in appendix 9. 5 out of 33 samples (4B, 3T, 12B, 13B and 11T) preserved the surface roughness through the whole process, which leads to a conclusion that the photogrammetric replication of rock joint surfaces has potential for further developing the methodology. However, there seems to be a long way to go before this method can be used effectively for cost reduction in derivation of parameters of mechanical behavior of large scale rock joints.

The photogrammetric modelling in the other hand seems to work quite effectively, and as the method is currently able to provide point density measures exceeding 40 points per mm^2, for a 170 x 60 (mm x mm) sample, the method offers high potential to be used for surface characterization and parametrization in the future.

Digital modeling and roughness characterization of rock surfaces has been a field of intensive developments in the past decade. These developments have produced a variety of methods for rock surface evaluation purposes. The methods applied in this thesis have different strengths and weaknesses, and at the end of the day, it’s all about choosing the right tool for the job at hand. As the job of this thesis was to develop metrics for surface evaluation for the photogrammetric replication of rock joint surfaces, the right tool for this would seem to be directional 3D roughness evaluation according to method presented by Tatone & Grasselli (2009). For the geometrical change it cannot be stressed enough, that the modelling of the replica samples was conducted post-shearing, and the geometrical change mapping cannot thus present the full truth about the effects of geometrical change in the replication process. The average effect of shearing is considered to be around 6 present, based on evaluation of directional 3D roughness analysis in appendix 9, the shear damages are regional, but the effective area varies between samples.

The digital representation of handheld profilometry and traditional JRC measurement, built in this thesis work seem to offer a good platform for building the digital surface characterization further, while comparing the surface characteristics with a large database of JRC measurements collected over the years by the academic community.

There is still plenty of work to be done for the photogrammetric replication of rock joint surfaces to become a trusted and effective research method. While the photogrammetric modelling and roughness characterization techniques applied in this thesis seem to be working rather well, there are some major issues in the evaluation procedure. Most importantly the replica samples were sheared prior to photogrammetric modelling, and while this might very well explain the issues seen in the directional 3D roughness analysis, the verification would require more replicas to be produced, modelled and analyzed. Alternatively the damaged areas could be eliminated from the surfaces, but this would require re-evaluating the measuring metrics as the whole surface is utilized in the suggested method for roughness characterization. Also it can be argued that the damaged zones are the zones of interest in the end, as those are the parts participating most in the shearing process. Additionally more elaborate inspection of the surface damages on shear samples with comparison of shear results could give indications on the performance of the shear samples.

Finally some suggestions for further work can be given: Comparison of the shear results from replica samples with corresponding shear results of real rock surfaces should state the performance of the replication process in a very detailed manner. Additionally, comparisons of photogrammetric modelling of KARMO, with structured light techniques applied actively on other research projects would give information on the applicability of the photogrammetric modelling in many research examples from all over the world.

7 Conclusions

The goal for this thesis work was split to three parts: Identify errors related to the developed photogrammetric replication process, develop a method for measuring digital accuracy of photogrammetric replication of rock joint surfaces, and formulate a recommendation for imaging configuration and photogrammetric replication of rock joint surfaces.

Errors are inspected with literature review of photogrammetric publications, and monitored in measuring method development. The specific details of photogrammetric modelling case have major effect on the particular errors involved in a specific case, but with the case specifics defined as in the KARMO project, the modelling point density seems to reach a saturation point with about 300 photographs spread evenly around the sample and in multiple layers. For the photogrammetric replication process; the scatter of results from 3D printing seems to have a fairly large effect on the reliability of the replication process, and the casting procedure seems to be twisting the contact surface of replica sample to induce contact only in the sides of the final shearing samples. However, with appropriate quality management, the photogrammetric replication process would seem to be capable of producing accurate replicas of the modelled surface.

The method that seems to be performing best for the digital accuracy measurement of the replication process is surface roughness characterization with directional three dimensional roughness characterization methodology as this method utilizes the whole surface area in the process. For preliminary inspections, the R_S-metric offers a method for rapid inspections of variability over the whole process. Validation of these measurements at current stage do however require measurements that can be verified with traditional hand-measurements, and the process is suggested to be conducted with digital roughness characterization procedure with two dimensional JRC metrics.

It is recommended to construct the imaging procedure so that the target surface can be modelled from all directions, and from multiple heights. The photography should be performed in an environment of constant and sufficient lighting, so that the pictures can be captured with fast shutter speed enabling hand held photography to produce precise images. Alternatively a rotational platform for the sample can be built, so that the

camera can be fixed on steady location and a slower shutter speed can be utilized. The alternative configuration would allow usage of lower ISO sensitivity in same lighting conditions. The alternative configuration is more laborious to build, but enables easier quality control and shooting protocol to be utilized. The saturation point for point density was achieved with around 300 pictures, taken with f-11, exposure time of 1/125 seconds and ISO value as 2000, spread evenly around the target surface in three layers corresponding to 30, 40 and 45 degrees from the horizontal plane. The high ISO value may inflict noise on the images, and a lower ISO value is recommended in the process. The verification of effects of ISO sensitivity is suggested for further study. The recommended configuration is to apply the following settings for the upcoming photogrammetry in photogrammetric replication of rock joint surfaces in the KARMO research project.

- Camera Canon EOS 600D DSLR
- Objective Canon EF 35mm f/2 IS USM
- F-stop so that whole surface area fits in the depth of field, e.g. f/16 for 2 m shooting distance for 1.7 m x 0.6 m surface
- Exposure time so that camera movement during a shot is infinitesimal, for hand held shooting, e.g. 1/125 s, and for shooting from a steady platform in the way that camera automatization allows the exposure time to expand without losing the center crosshair in the shoot.
- Lighting as constant, and as high as reasonably possible, for example at 5000 lx
- Image quantity as 300
- Imaging angles as 30, 45 and 60 degrees from horizontal plane
- Imaging locations evenly spread around the sample

8 References

Aalto University. 2014, KARMO II – Kallion rakopintojen mekaaniset ominaisuudet, Tutkimushanke-esitys.

Manual of photogrammetry, 1980, American Society of Photogrammetry, Falls Church VA.

Barton, N & Choubey, V. 1978, Shear strength of rock joints in theory and practice, *International journal of rock mechanics and mining sciences & geomechanics abstracts*, vol. 15, no. 3, pp. 51-51.

Arya, S., Mount, D., Netanyahu, N., Silverman, R. & Wu, A. 1998, An optimal algorithm for approximate nearest neighbor searching in fixed dimensions, *Journal of the Association for Computing Machinery*, vol. 45, no. 6, pp. 891-923.

Atkinson, K.B. 2001, *Close range photogrammetry and machine vision*, Whittles Publishing, Latheronwheel.

Baker, B.R., Gessner, K., Holden. E. and Squelch, A. 2008. Automatic detection of anisotropic features on rock surfaces, Geosphere; April 2008; v. 4; no. 2; pp. 418-428

Bandis, S., Lumsden, A. & Barton, N. 1981, Experimental studies of scale effects on the shear behaviour of rock joints, *International journal of rock mechanics and mining sciences & geomechanics abstracts*, Elsevier.

Bandis, S. 1980, *Experimental studies of scale effects on shear strength, and deformation of rock joints*, University of Leeds.

Barton, N. & Bandis, S. 1982, Effects of block size on the shear behavior of jointed rock, *The 23rd US Symposium on Rock Mechanics (USRMS)*, American Rock Mechanics Association.

Barton, N & Bandis, S. 1990, Review of predictive capabilities of JRC-JCS model in engineering practice. In N. Barton & O. Stephansson, Rock Joints: Proceedings of the International Symbosium on Rock Joints, Loen, Norway: 603-610. Rotterdam: A.A. Balkema.

Barton, N. & Choubey, V. 1977, The shear strength of rock joints in theory and practice, *Rock Mechanics and Rock Engineering*, vol. 10, no. 1, pp. 1-54.

Bertin, S., Friedrich, H., Delmas, P., Chan, E. & Gimel'Farb, G. 2014, DEM quality assessment with a 3D printed gravel bed applied to stereo photogrammetry, *Photogrammetric Record*, vol. 29, no. 146, pp. 241-264.

Brasington, J., Smart, R.M.A., Lane, S.N. & Chandler, J.H. 2003, Close range digital photogrammetric analysis of experimental drainage basin evolution, *Earth Surface Processes and Landforms*, vol. 28, no. 3, pp. 231-247.

Brown, D.C. 1979, The bundle adjustment – progress and prospects. International Archives of Photogrammetry, 21(3), ISP Congress, Helsinki, pp. 1-33.

Butler, J.B., Lane, S.N. & Chandler, J.H. 1998, Assessment of Dem Quality for Characterizing Surface Roughness Using Close Range Digital Photogrammetry, *Photogrammetric Record,* vol. 16, no. 92, pp. 271-291.

Chandler, J., Buffinbélanger, T., Rice, S., Reid, I. & Graham, D. 2003, The accuracy of a river bed moulding/casting system and the effectiveness of a low-cost digital camera for recording river bed fabric, *Photogrammetric Record,* vol. 18, no. 103, pp. 209-223.

Chae, B.G., Ichikawa, Y., Jeong, G. C., Seo, Y.S., and Kim, B.C. 2004. Roughness measurement of rock discontinuities using a confocal laser scanning microscope and the Fourier spectral analysis. *Engineering Geology*, (72) 3-4, pp. 181-199

Cooper, M.A.R. & Cross, P.A. 1988, Statistical concept and their application in photogrammetry and surveying, *Photogrammetric Record,* vol. 12, no. 71, pp. 637-663.

Cross, P. 1983, Advanced least squares applied to position-fixing*, North East London Polytechnic, Department of Land Surveying, Working Paper,* [Online], vol. 6

Cross, P. 1990, Working Paper No. 6, Advanced least squares applied to position-fixing. Department of Land Surveying, Polytechnics of East London p. 205.

Dimitrov, D. & Klaus, K. 2010, *Geometric applications of principal component analysis : Geometrische Anwendungen der Hauptkomponentenanalyse*, Berlin: Freie Universität Berlin Universitätsbibliothek.

El-Soudani, S. 1978, Profilometric analysis of fractures, *Metallography,* vol. 11, no. 3, pp. 247-336.

Fardin, N., Stephansson, O. & Jing, L. 2001, The scale dependence of rock joint surface roughness, *International Journal of Rock Mechanics and Mining Sciences,* vol. 38, no. 5, pp. 659-669.

Fardin, N., Feng, Q. & Stephansson, O. 2004, Application of a new in situ 3D laser scanner to study the scale effect on the rock joint surface roughness, *International Journal of Rock Mechanics and Mining Sciences,* vol. 41, no. 2, pp. 329-335.

Fischler, M., Bolles, R. & Foley, J.D. 1981, Random Sample Consensus: A Paradigm for Model Fitting with Applications to Image Analysis and Automated Cartography, *Communications of the ACM,* vol. 24, no. 6, pp. 381-395.

Fischler, M.A., Bolles, R.C. 1986. Random Sample Consensus: a paradigm for model fitting with applications to image analysis and automated cartography. In: Martin, A.F., Oscar, F. Readings in Computer Vision: Issues, Problems, Principles and Paradigms. Morgan Kaufmann Publishers Inc., London, pp. 726-740.

Fletcher, R. 1987, *Practical methods of optimization*, Chichester: Wiley ; New York: Wiley.

Fryer, J. 2007, *Applications of 3D measurement from images.*

Furukawa, Y. 2007, Accurate, Dense, and Robust Multi-View Stereopsis, *2007 IEEE Conference on Computer Vision and Pattern Recognition*, pp. 1-8.

Furukawa, Y. 2010, Towards Internet-scale multi-view stereo, *2010 IEEE Computer Society Conference on Computer Vision and Pattern Recognition*, pp. 1434-1441.

Gentier, S., Riss, J., Archambault, G., Flamand, R., and Hopkins, D. 2000. Influence of fracture geometry on shear behavior. *International Journal of Rock Mechanics and Mining Science*, (37) 1-2, pp. 161-174.

Gill, P.E., Murray, W. & Wright, M.H. 1981, "Practical optimization".

Grasselli, G., Wirth, J. & Egger, P. 2002, Quantitative three-dimensional description of a rough surface and parameter evolution with shearing, *International Journal of Rock Mechanics and Mining Sciences,* vol. 39, no. 6, pp. 789-800.

Girardeau-Montaut, D. 2014. Cloud Compare Documentation. Available at http://www.danielgm.net/cc/, accessed on May 28 2015.

Grasselli, G. & Egger, P. 2003, Constitutive law for the shear strength of rock joints based on three-dimensional surface parameters, *International Journal of Rock Mechanics and Mining Sciences,* vol. 40, no. 1, pp. 25-40.

Haberfield, C.M. & Johnston, I.W. 1994. A mechanistically-based model for rough joints. *International Journal of Rock Mechanics and Mining Science & Geomechanics Abstracts*, (31) 4, pp, 279-292.

Haneberg, W.C. 2008, Using close range terrestrial digital photogrammetry for 3-D rock slope modeling and discontinuity mapping in the United States, *Bulletin of Engineering Geology and the Environment,* vol. 67, no. 4, pp. 457-469.

Haneberg, W.C. 2007, Directional roughness profiles from three-dimensional photogrammetric or laser scanner point clouds, *E. Eberhardt, D. Stead, &T. Morrison (eds.), Rock Mechanics: Meeting Society's Challenges and Demands*, pp. 101.

Heikkinen, J. 2005, *The circular imaging block in close-range photogrammetry.* Teknillinen korkeakoulu, Espoo.

Hencher, S., Toy, J. & Lumsden, A. 1993, Scale dependent shear strength of rock joints, *Scale effects in rock masses,* vol. 93, pp. 233-240.

Hodge, R., Brasington, J. & Richards, K. 2009, In situ characterization of grain-scale fluvial morphology using Terrestrial Laser Scanning, *Earth Surface Processes and Landforms*, vol. 34, no. 7, pp. 954-968.

Hong, E. S., Lee, I. M., & Lee, J. S., 2006. Measurement of rock joint roughness by 3D scanner.*Geotechnical Testing Journal*, (29)6: 482-489.

International Society for Rock Mechanics Comission on Standardization of laboratory and Field Tests. 1978. Suggested methods for the quantative description of discontinuities in rock masses. *International Journal of Rock Mechanics and Mining Sience and Geomechanics.* Abstracts. 15, pp. 219-368

Kallio, P. 2015. Rakopinnan karkeuden mittaaminen fotogrammetrisesti. Bachelor's thesis. Aalto University.

Kutter, H. & Otto, F. 1990, Influence of parallel and cross joints on shear behaviour of rock discontinuities, *Proc.Rock Joints.Loen, Norway, ,* pp. 243-250.

Lanaro, F. 2000, A random field model for surface roughness and aperture of rock fractures, *International Journal of Rock Mechanics and Mining Sciences,* vol. 37, no. 8, pp. 1195-1210.

Lane, S.N. 2000, Application of Digital Photogrammetry to Complex Topography for Geomorphological Research, *Photogrammetric Record,* vol. 16, no. 95, pp. 793-821.

Lee, H.-S., & Ahn, K.-W. 2004. A prototype of digital photogrammetric algorithm for estimating roughness of rock surface. *Geoscience Journal*, (8)3, 333-341.

Lowe, D.G. 2004, Distinctive image features from scale-invariant keypoints, *International Journal Of Computer Vision,* vol. 60, no. 2, pp. 91-110.

Lowe, D.G. 1999, Object recognition from local scale-invariant features, *Proceedings of the Seventh IEEE International Conference on Computer Vision,* vol. 2, pp. 1150-1157.

Luhmann, T. 2011, *Close range photogrammetry : principles, methods and applications,* Whittles Publishing.

Maerz, N.H., Franklin, J.A. and Bennett, C.P. 1990. Joint roughness measurement using shadow profilometry, *International Journal of Rock Mechanics and Mining Sience and Geomechanics*. Abstracts, 27(5), pp. 329-343.

Malinverno, A. 1990, A simple method to estimate the fractal dimension of a self-affine series, *Geophysical Research Letters,* vol. 17, no. 11, pp. 1953-1956.

Mikhail, E.M. 1976, *Observations and least squares,* New York: IEP.

Mikhail, E.M. & Gracie. 1981, Analysis & Adjustment of Survey Measurements. Van Nostrand Reinhold Company, p. 368.

Myers, N. 1962, Characterization of surface roughness, *Wear*, vol. 5, no. 3, pp. 182-189.

Nasseri, M.H.B., Tatone, B.S.A., Grasselli, G., and Young, R.P. 2009. Fracture toughness and fracture roughness interrelationship in thermally treated Westerly granite. *Pure and Applied Geophysics*.

Nocedal, J., Wright, S.J. 1999. Numerical Optimization. Springer, New York.

Rahman, Z., Slob, S. and Hack, R. 2006. Deriving roughness characteristics of rock mass discontinuities from terrestrial laser scan data, IAEG2006 Paper number 437.

Seidel, J.P., Haberfield, C.M. 2002. A theoretical model for rock joints subjected to constant normal stiffness derect shear. *International Journal of Rock Mechanics and Mining Sciences*, (39) 5, pp. 539-553.

Szeliski, R. & Kang, S.B. 1994, Recovering 3D shape and motion from image streams using nonlinear least squares, *Journal of Visual Communication and Image Representation*, vol. 5, no. 1, pp. 10-28.

Tatone, B.S. & Grasselli, G. 2013, An investigation of discontinuity roughness scale dependency using high-resolution surface measurements, *Rock Mechanics and Rock Engineering*, vol. 46, no. 4, pp. 657-681.

Tatone, B.S. & Grasselli, G. 2012, Quantitative measurements of fracture aperture and directional roughness from rock cores, *Rock Mechanics and Rock Engineering*, vol. 45, no. 4, pp. 619-629.

Tatone, B.S. & Grasselli, G. 2009, A method to evaluate the three-dimensional roughness of fracture surfaces in brittle geomaterials, *Review of scientific instruments*, vol. 80, no. 12, pp. 125110.

Tatone, B. 2009. Quantative Characterization of Natural Rock Discontinuity Roughness *In-Situ* and in the Laboratory. Master's thesis. University of Toronto.

Tatone, B. 2013, An Investigation of Discontinuity Roughness Scale Dependency Using High-Resolution Surface Measurements, *Rock Mechanics and Rock Engineering*, vol. 46, no. 4, pp. 657-681.

Tolvanen, L. 2015. Itsetiivistyvä betoninen jäljennysmateriaali rakopinnoille. Bachelor's thesis. Aalto University.

Triggs, B., McLauchlan, P. F., Hartley, R. I., & Fitzgibbon, A. W. (2000). Bundle adjustment—a modern synthesis. In *Vision algorithms: theory and practice* (pp. 298-372). Springer Berlin Heidelberg.

Tse, R. & Cruden, D. 1979, Estimating joint roughness coefficients, *International journal of rock mechanics and mining sciences & geomechanics abstracts*, Elsevier, pp. 303.

Westoby, M.J., Brasington, J. Glasser, N.F., Hambrey, M.J., Reynolds, J.M. 2012. 'Structure-from-Motion' photogrammetry: A low-cost, effective tool for geosience applications. Geomerphology 179, pp. 300-314. Elsevier B.V.

Wolf, P.R. 1997, Adjustment computations: statistics and least squares in surveying and GIS.

Wright, S.J. & Nocedal, J. 1999, *Numerical optimization,* Springer New York.

Wu, C. 2013, Towards Linear-time Incremental Structure from Motion, *2013 International conference on 3D vision (3DV 2013),* pp. 127-134.

Wu, C., Agarwal, C. Cureless, B. and Seitz, S.M. 2011. Multicore Bundle Adjustment. In CVPR.

Yang, Z.Y., Chiang, D.Y. 2000. An experimental study on the progressive shear behavior of rock joints with tooth-shaped asperities. *International Journal of Rock Mechanics and Mining Sciences,* (37) 8, pp. 1247-1259.

Yu, X. & Vayssade, B. 1991, Joint profiles and their roughness parameters, *International journal of rock mechanics and mining sciences & geomechanics abstracts*Elsevier, , pp. 333.

Appendices

Appendix 1.JRC curves. 1 pages.

Appendix 2. JRC Amplitude.1 pages.

Appendix 3. JRC measurements from replica samples. 1 pages.

Appendix 4. JRC and amplitude measures for original rock slab. 1 pages.

Appendix 5. 3D printing settings used in pilot mold production. 1 pages.

Appendix 6. JRC measurements. 2 pages.

Appendix 7. Comparison of casting mold roughness (Rs) for bottom and top samples. 2 pages.

Appendix 8. Surface roughness evaluation with Rs-metrics. 2 pages.

Appendix 9. Directional roughness analysis. 3 pages.

Appendix 1. JRC curves

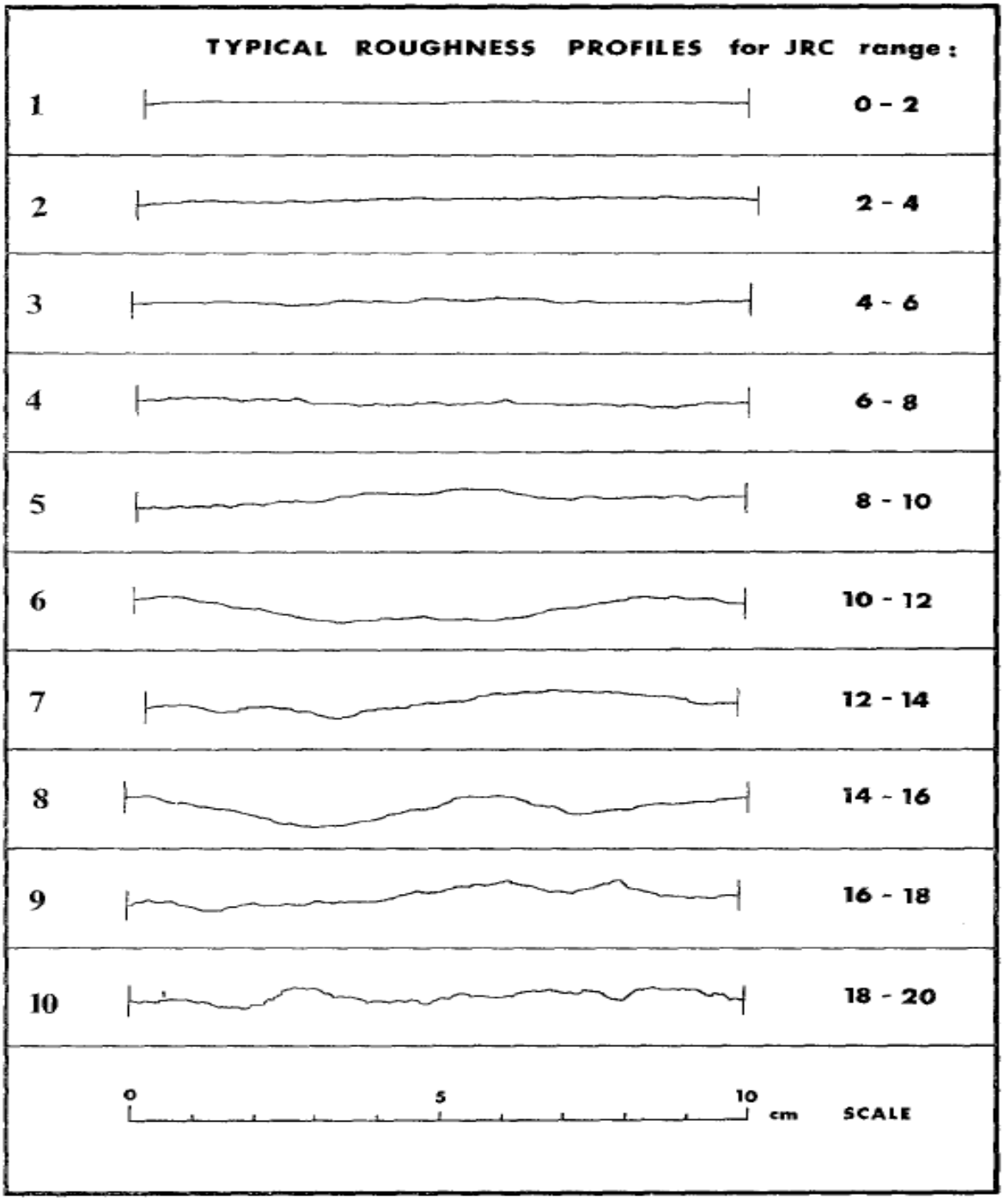

Figure 42. Example joint surface profiles for different JRC values (Barton & Choubey, 1977)

Appendix 2. JRC amplitude

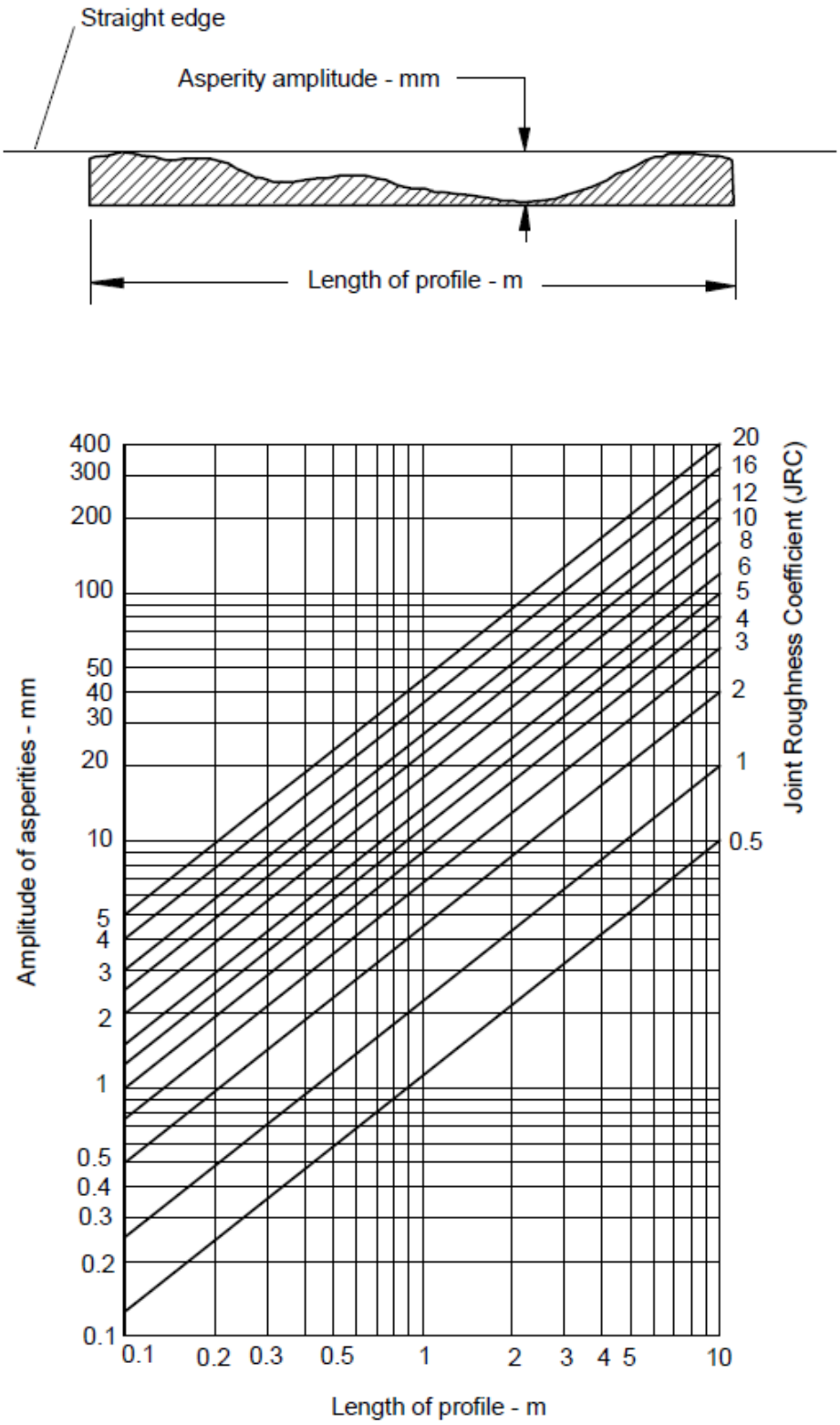

Figure 43. Diagram by Barton (1981) to estimate the JRC values using the asperity amplitude and length of rock joint. Figure is redesigned by (Hoek 2015)

Appendix 3. JRC measurements from replica samples

Table 5. JRC measurements from replica samples for measuring lines 1-6, adapted from Kallio, 2015

Sample ID	1.	2.	3.	4.	5.	6.
10x1T	2	2	2	3	2	3
10x1B	2	3	2	2	2	3
7.5x2T	4	3	3	2	2	2
7.5x2B	3	3	3	4	3	2
7.5x3T	3	3	3	2	4	2
7.5x3B	3	4	4	3	4	2
7.5x4T	3	4	3	2	2	2
7.5x4B	3	4	3	3	3	3
7.5x5T	4	3	3	3	3	2
7.5x5B	3	3	3	3	4	2
5x6T	5	5	5	4	5	4
5x6B	4	5	4	4	5	4
5x7T	4	5	4	4	4	5
5x7B	4	5	4	4	5	5
5x8B	5	4	4	6	4	4
5x8T	6	4	4	2	3	3
5x9T	5	5	6	2	3	4
5x9B	5	6	6	4	4	4
2.5x10T	6	6	6	4	5	5
2.5x10B	6	5	6	6	6	6
2.5x11T	5	6	5	4	6	5
2.5x11B	6	6	5	4	5	3
2.5x12T	6	6	5	5	4	3
2.5x12B	5	6	6	4	4	4
2.5x13T	5	6	6	6	6	7
2.5x13B	6	9	7	6	5	7
1x14T	9	9	9	6	7	6
1x14B	8	9	9	6	7	6
1x15T	7	8	10	9	8	11
1x15B	8	10	11	11	6	11
1x16T	11	9	10	6	9	11
1x16B	10	11	10	7	7	10
1x17T	13	12	11	5	9	11
1x17B	11	12	10	5	9	11

Appendix 4. JRC and amplitude measures for original rock slab.

Table 6. Segmented JRC and amplitude measures from the rock slab.

Longnitual lines											
Seqment	1	2	3	4	5	6	7	8	9	10	**Average**
Line 1											
JRC	13	13	10	12	14	14	14	12	11	14	12.7
Amplitude	4.48	4.39	4.55	5.1	4.18	3.24	4.91	8.65	3.13	4.07	
Line 2											
JRC	10	11	14	11	12	13	15	12	13	12	12.3
Amplitude	3.6	4.73	4.92	3.76	4.55	4.07	4.19	6.26	5.39	4.92	
Line 3											
JRC	11	11	11	12	14	11	11	11	13	13	11.8
Amplitude	2.44	3.05	3.41	3.6	4.14	3.44	4.68	2.94	3.43	5.8	
										Average	**12.3**
Latitudal lines											
Line 4											
JRC	8	11	9	10	9	9	11	12	8	12	9.9
Amplitude	1.56	2.72	1.55	1.45	1.53	1.84	2.59	2.99	1.68	4.61	
Line 5											
JRC	7	6	9	8	7	10	7	10	10	11	8.5
Amplitude	2.1	1.46	1.96	1.25	1.42	1.97	2.23	3.01	3.02	1.86	
Line 6											
JRC	10	10	10	10	10	10	10	10	11	10	10.1
Amplitude	1.1	2.15	2.98	2.34	2.67	1.61	1.93	2.42	3.62	1.77	
										Average	**9.5**

Table 7. Amplitude measures from rock slab, and corresponding JRC values.

Line	Amplitude	JRC
1	13,48	3
2	17,65	4
3	16,62	4
4	8,13	6
5	7,38	5
6	9,30	6

Appendix 5. 3D printing settings used in pilot mold production

Parameter	Value	Notes
layer height	0.050 mm	20 layers per mm
shell thickness	1.000 mm	perimeter
bottom/top	1.000 mm	
fill density	20 %	rectilinear
print speed	50 mm/s	
nozzle temperature	215 C	for polylactic acid
bed temperature	70 C	for polylactic acid
adhesion type	brim	20 lines
stitching	keep open faces	disables stitching

Appendix 6. JRC measurements

Table 8. Hand measured JRC for replicas

Sample ID	1.	2.	3.	4.	5.	6.
7.5x2B	3	3	3	4	3	2
7.5x3B	3	4	4	3	4	2
7.5x4B	3	4	3	3	3	3
7.5x5B	3	3	3	3	4	2
5x6B	4	5	4	4	5	4
5x7B	4	5	4	4	5	5
5x8T	6	4	4	2	3	3
5x9B	5	6	6	4	4	4
2.5x10B	6	5	6	6	6	6
2.5x11B	6	6	5	4	5	3
2.5x12B	5	6	6	4	4	4
2.5x13B	6	9	7	6	5	7
1x14B	8	9	9	6	7	6
1x15B	8	10	11	11	6	11
1x16B	10	11	10	7	7	10
1x17B	11	12	10	5	9	11

Table 9. Hand measured JRC for casting molds

Sample ID	1.	2.	3.	4.	5.	6.
7.5x2B	3	2	3	2	1	2
7.5x3B	4	4	3	2	3	1
7.5x4B	2	2	2	2	1	2
7.5x5B	3	3	2	1	2	1
5x6B	4	4	4	3	3	3
5x7B	5	5	5	4	2	5
5x8B	6	6	4	3	2	3
5x9B	5	6	6	2	3	4
2.5x10B	9	7	8	6	7	7
2.5x11B	6	7	4	3	8	5
2.5x12B	5	6	7	3	2	2
2.5x13B	7	8	7	5	4	6
1x14B	9	9	11	6	8	7
1x15B	6	7	9	7	7	8
1x16B	8	8	5	4	7	6
1x17B	10	11	10	5	9	10

Table 10. Hand measured JRC for original rock slab

Sample ID	1.	2.	3.	4.	5.	6.
7.5x2B	9	10	10	9	10	9
7.5x3B	10	9	9	9	10	9
7.5x4B	9	9	9	10	10	9
7.5x5B	9	9	9	9	9	9
5x6B	10	9	10	9	9	10
5x7B	9	10	12	10	10	11
5x8B	12	11	9	9	8	9
5x9B	9	10	11	9	9	9
2.5x10B	12	13	11	8	9	8
2.5x11B	9	11	10	8	11	7
2.5x12B	10	12	11	9	8	9
2.5x13B	11	12	11	14	11	10
1x14B	9	12	13	6	7	7
1x15B	8	10	13	8	10	12
1x16B	8	9	7	8	8	7
1x17B	15	12	9	6	9	8

Appendix 7. Comparison of casting mold roughness (Rs) for bottom and top samples.

Sample ID	Difference	Difference / roughness of bottom sample
1	0,0028	0,28 %
2	0,0083	0,82 %
3	0,0019	0,19 %
4	0,0063	0,63 %
5	0,0005	0,05 %
6	0,0025	0,24 %
7	0,0067	0,64 %
8	0,0230	2,27 %
9	0,0214	2,06 %
10	0,0105	1,01 %
11	0,0395	3,74 %
12	0,0057	0,56 %
13	0,0002	0,02 %
14	0,0189	1,78 %
16	0,0006	0,06 %
17	0,0399	3,74 %

Appendix 8. Surface roughness evaluation with Rs-metrics

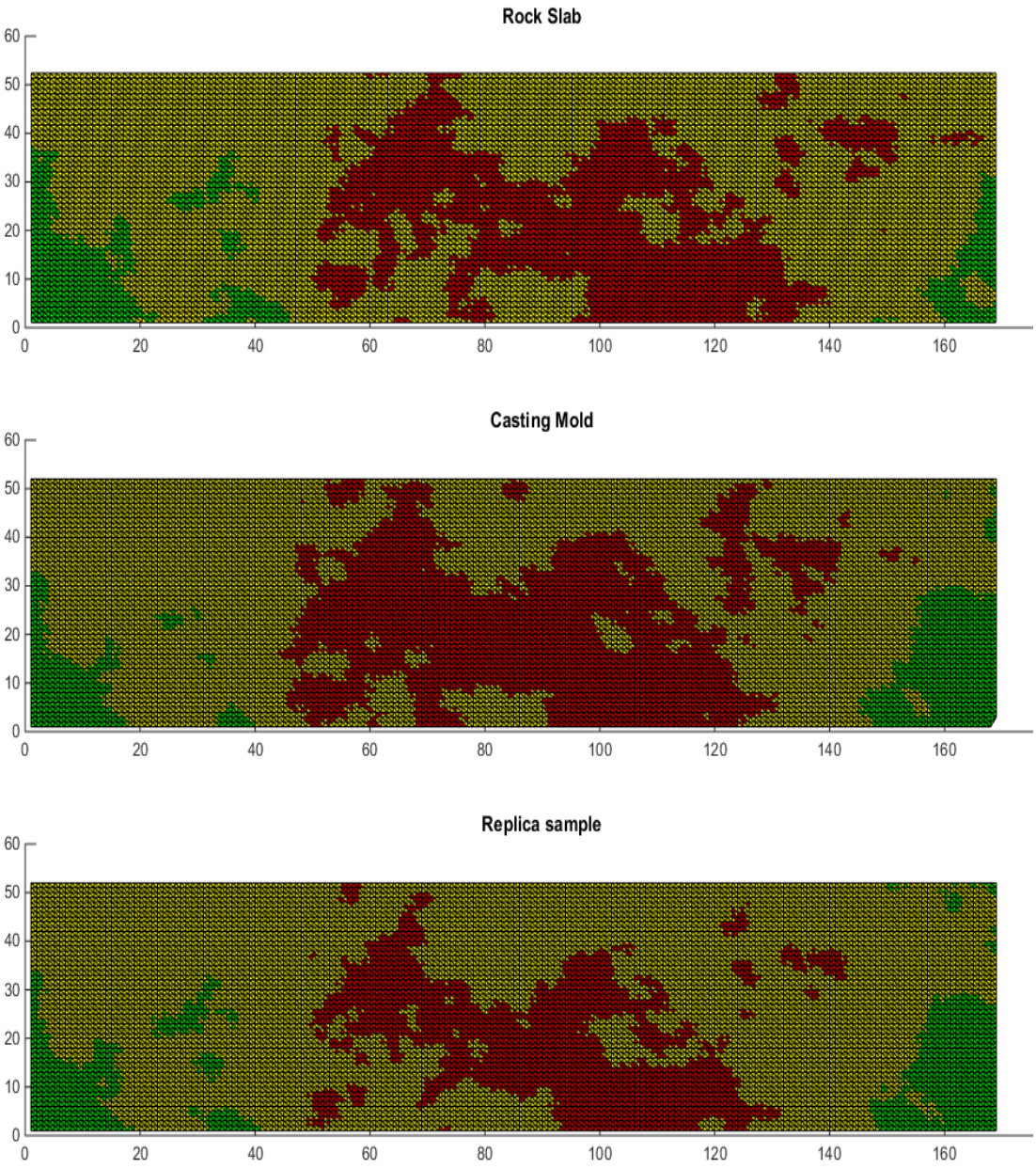

Figure 44. Surface roughness by Rs-metrics presented for 'good example', sample 11T. Red color illustrates high elevation, yellow intermediate elevation, and green a low elevation measured from lowest point of the surface.

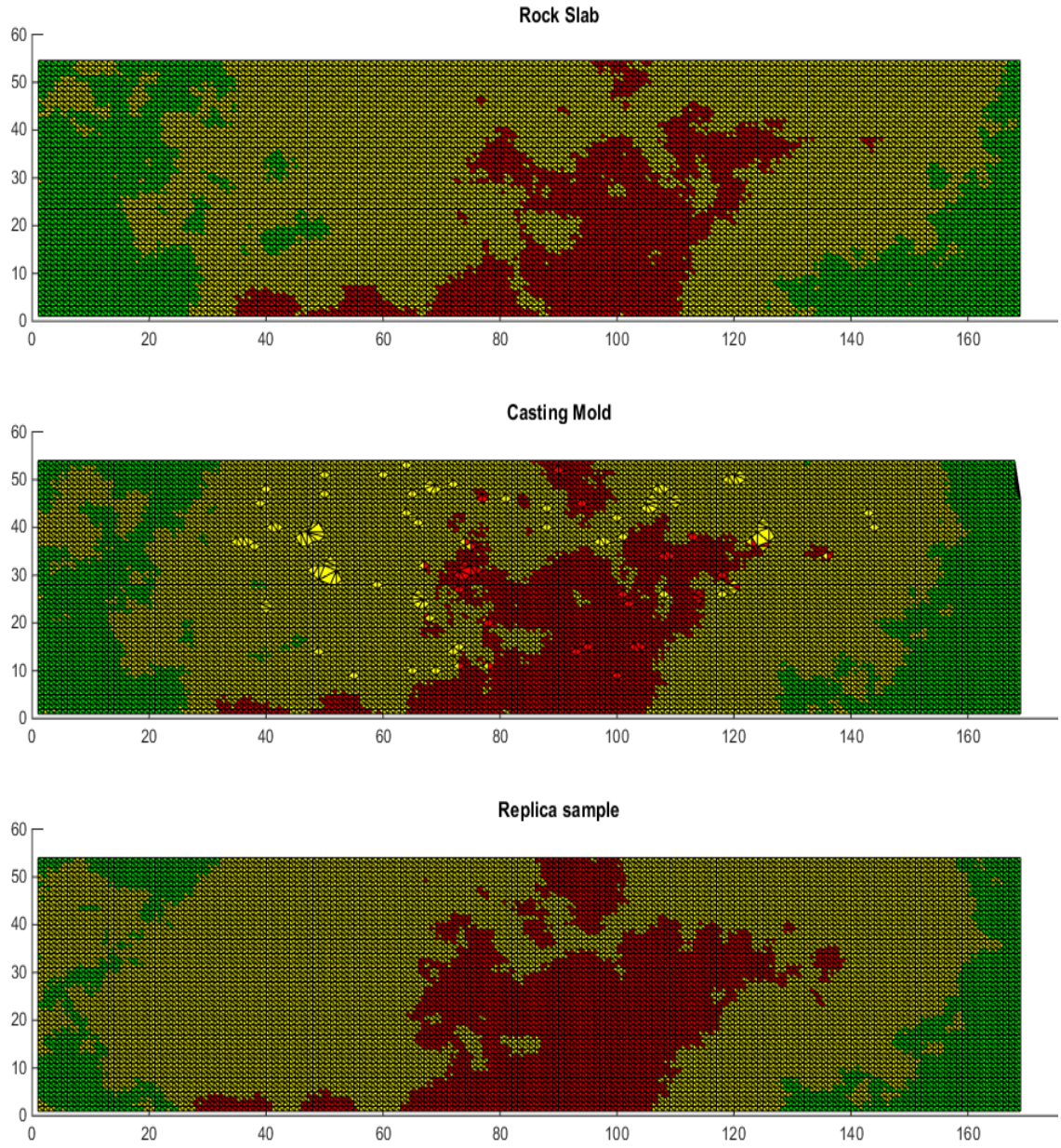

Figure 45. Surface roughness by Rs-metrics presented for 'bad example', sample 7T. Red color illustrates high elevation, yellow intermediate elevation, and green a low elevation measured from lowest point of the surface.

Appendix 9. Directional roughness analysis for all replication samples, presented as polar plot, with roughness as distance from center point, and angle of roughness measurement as deviation from picture north in clockwise direction.

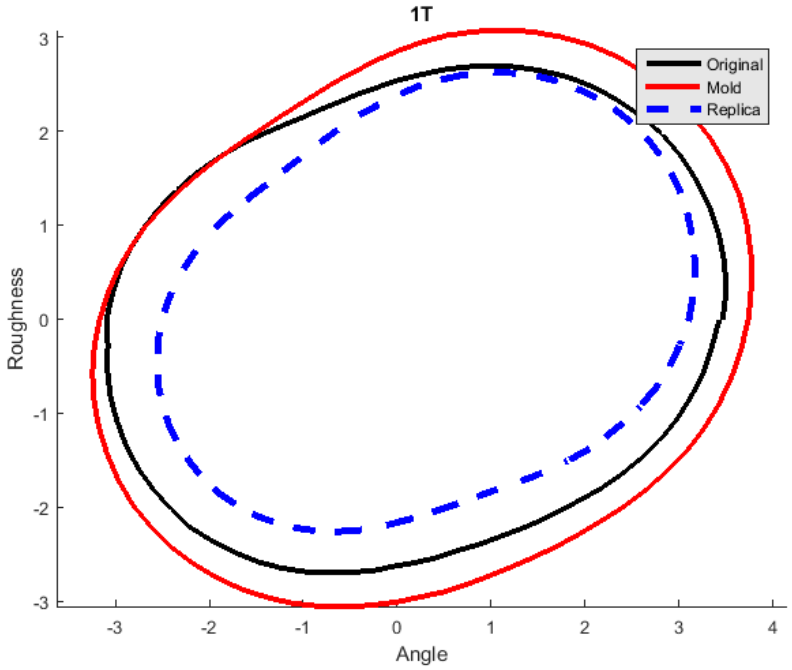

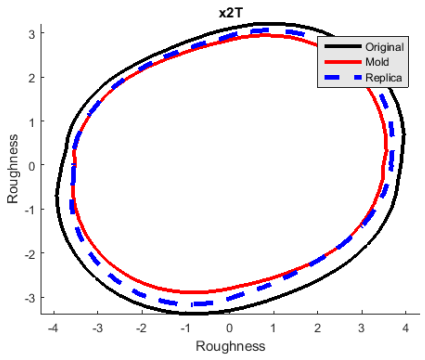

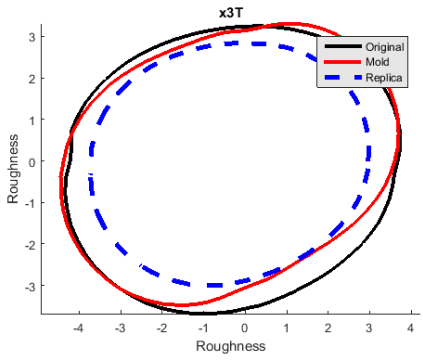

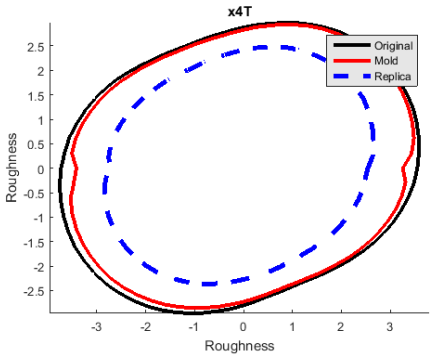

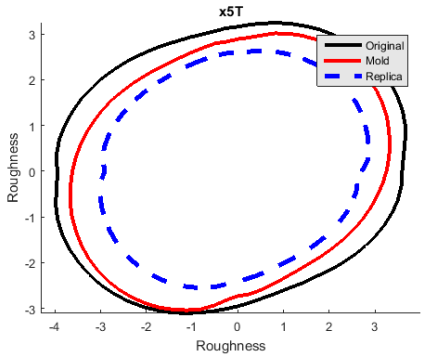

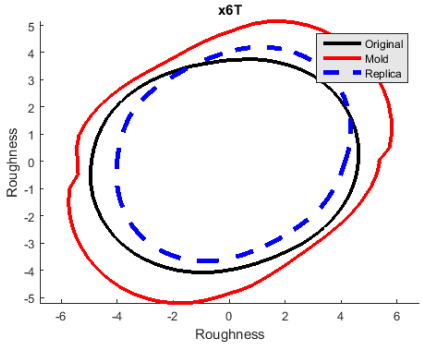
x6T
Original
Mold
Replica
Roughness
Roughness

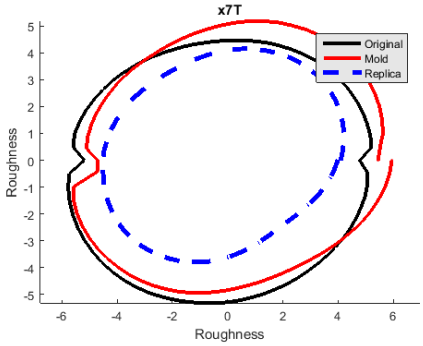
x7T
Original
Mold
Replica
Roughness
Roughness

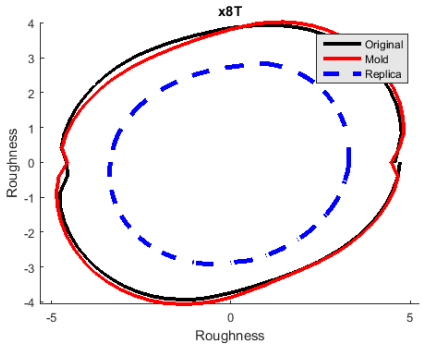
x8T
Original
Mold
Replica
Roughness
Roughness

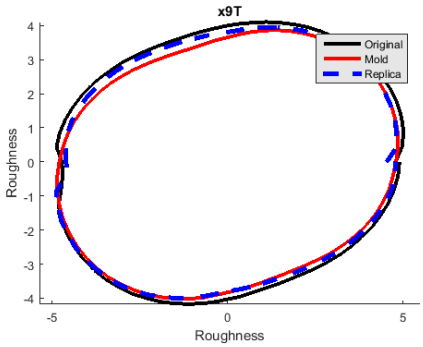
x9T
Original
Mold
Replica
Roughness
Roughness

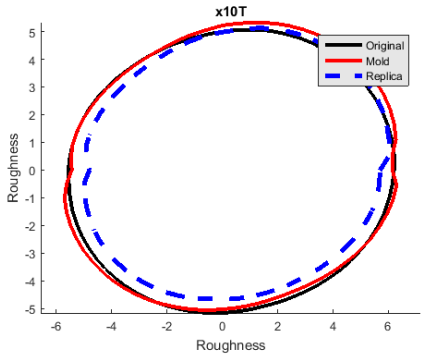
x10T
Original
Mold
Replica
Roughness
Roughness

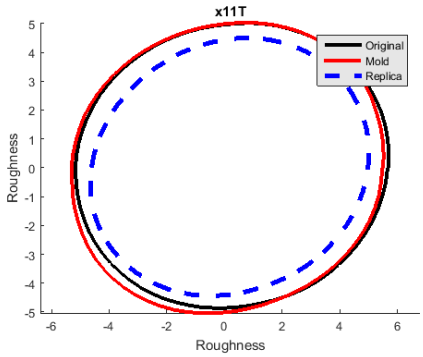
x11T
Original
Mold
Replica
Roughness
Roughness

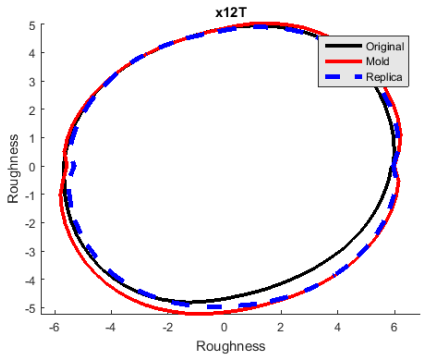
x12T
Original
Mold
Replica
Roughness
Roughness

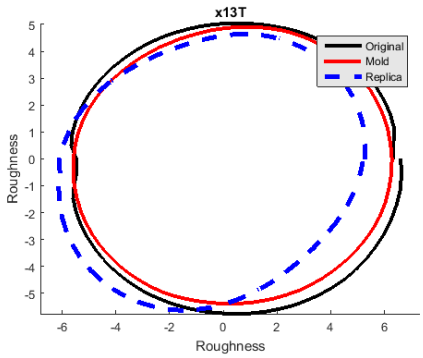
x13T
Original
Mold
Replica
Roughness
Roughness

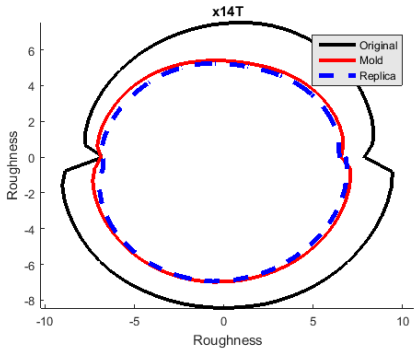
x14T
Original
Mold
Replica
Roughness
Roughness

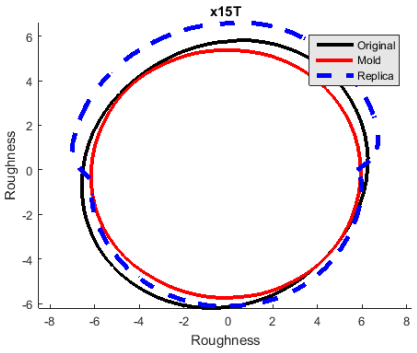
x15T
Original
Mold
Replica
Roughness
Roughness

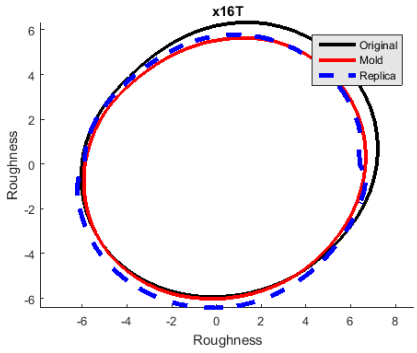
x16T
Original
Mold
Replica
Roughness
Roughness

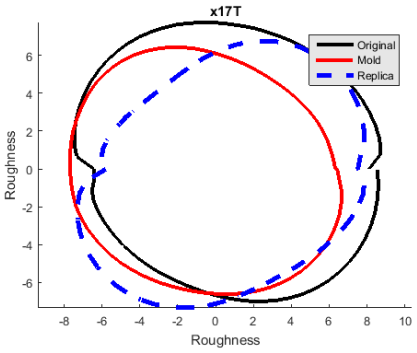
x17T
Original
Mold
Replica
Roughness
Roughness